Star clusters in tidal debris

Michael Rodruck,[1,2]★ Jane Charlton,[1] Sanchayeeta Borthakur,[3] Aparna Chitre,[4] Patrick R. Durrell,[5] Debra Elmegreen,[6] Jayanne English,[7] Sarah C. Gallagher,[8] Caryl Gronwall,[1,9] Karen Knierman,[3] Iraklis Konstantopoulos,[10] Yuexing Li,[1] Moupiya Maji,[11] Brendan Mullan,[12] Gelys Trancho[13] and William Vacca[14]

[1]*Department of Astronomy and Astrophysics, The Pennsylvania State University, University Park, PA 16802, USA*
[2]*Department of Physics, Engineering, and Astrophysics, Randolph-Macon College, Ashland, VA 23005, USA*
[3]*School of Earth and Space Exploration, Arizona State University, 550 E. Tyler Mall, Room PSF-686 (PO Box 871404), Tempe, AZ 85287, USA*
[4]*Space Telescope Science Institute, 3700 San Martin Drive, Baltimore, MD 21218, USA*
[5]*Department of Physics, Astronomy, Geology and Environmental Sciences, Youngstown State University, Youngstown, OH 44555, USA*
[6]*Department of Physics and Astronomy, Vassar College, Poughkeepsie, NY 12604, USA*
[7]*Department of Physics and Astronomy, University of Manitoba, Winnipeg, MB R3T 2N2, Canada*
[8]*Department of Physics and Astronomy and Institute for Earth and Space Exploration, University of Western Ontario, London, ON N6A 3K7, Canada*
[9]*Institute for Gravitation and the Cosmos, The Pennsylvania State University, University Park, PA 16802, USA*
[10]*Independent Scholar, Wellington, New Zealand*
[11]*Inter-University Centre for Astronomy and Astrophysics (IUCAA), Post Bag 4, Ganeshkhind, Pune 411 007, India*
[12]*Department of Natural Sciences and Engineering Technology, Point Park University 201 Wood St, Pittsburgh, PA 15222, USA*
[13]*Thirty Meter Telescope International Observatory, 100 W Walnut St, #300, Pasadena, CA 91124, USA*
[14]*SOFIA-USRA, NASA Ames Research Center, MS N232-12, Moffett Field, CA 94035, USA*

ABSTRACT

We present results of a *Hubble Space Telescope* (*HST*) *UBVI*-band study of star clusters in tidal tails, using new WFC3 and ACS imaging to complement existing WFPC2 data. We survey 12 tidal tails across seven merging systems, deriving ages and masses for 425 star cluster candidates (SCCs). The stacked mass distribution across all systems follows a power law of the form $\mathrm{d}N/\mathrm{d}M \propto M^{\beta}$, with $\beta = -2.02 \pm 0.15$, consistent with what is seen in other star-forming environments. *GALEX* and *Swift* UV imaging provide star formation rates (SFRs) for our tidal tails, which when compared with ages and masses of our SCCs, allows for a determination of the cluster formation efficiency (CFE). We find the CFE increases with increasing SFR surface density, matching the theoretical model. We confirm this fit down at SFR densities lower than previously measured (log Σ_{SFR} ($M_{\odot}$ yr^{-1} kpc^{-2}) ≈ -4.2), as related to the CFE. We determine the half-light radii for a refined sample of 57 SCCs with our *HST* WFC3 and ACS imaging, and calculate their dynamical age, finding the majority of them to be gravitationally bound. We also provide evidence of only low-mass ($<10^4\ M_{\odot}$) cluster formation in our nearest galaxy, NGC 1487, consistent with the theory that this system is a dwarf merger.

Key words: galaxies: interactions – galaxies: star clusters: general – galaxies: star formation.

1 INTRODUCTION

The gravitational origin of tidal tails was first realized with the pivotal work by Toomre & Toomre (1972), who showed that galactic tidal tails and warped discs could be simulated as gravitational encounters with another galaxy. In a very forward thinking section of their work, they suggested that galaxy mergers may be able to produce large amounts of star formation. This prediction was later borne out with the discovery of luminous infrared galaxies (LIRGs), made possible with the launch of the IR telescope *IRAS*. *IRAS* found that many galaxies with high ($>10^{11}$ L$_{\odot}$) IR luminosities have disturbed morphologies, indicative of past merging events (Sanders et al. 1988).

The IR emission of these LIRGs suggested star formation rates (SFRs) on the order of 100 M$_{\odot}$ yr^{-1} (Schweizer 1987).

Galaxy mergers can produce collisions between clouds of gas, which can provoke star formation. The high pressures generated in these collisions will lead to enhanced star formation efficiency (Jog & Solomon 1992) and the formation of massive star clusters (Zubovas, Sabulis & Naujalis 2014; Maji et al. 2017). Additionally, cloud collisions may provide external pressure to young clusters, keeping their contents gravitationally bound, preventing their destruction (Elmegreen 2008). The advent of high-resolution imaging, possible with *Hubble Space Telescope* (*HST*), has found evidence of such massive clusters within the interiors of merging galaxies in the form of bright, blue, compact objects (e.g. Whitmore et al. 1993; Whitmore & Schweizer 1995; Zepf et al. 1999). These objects, labelled as young massive clusters (YMCs), show properties similar
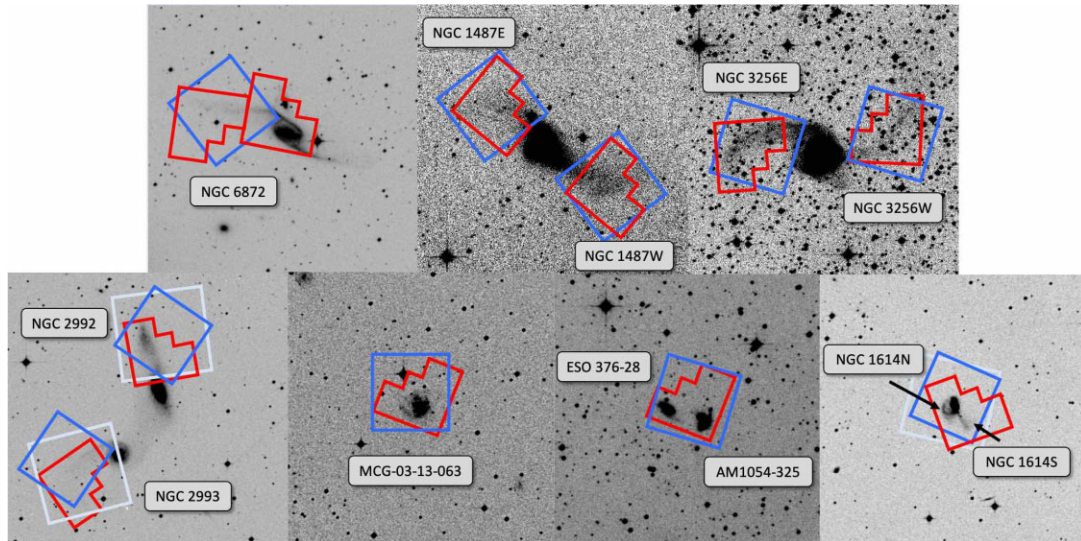
★ E-mail: mrodruck@gmail.com

Figure 1. Snapshots of our sample from the Digitized Sky Survey. Red outlines indicate WFPC2 pointings from Mullan et al. (2011) and Knierman et al. (2003). Blue and cyan squares show the WFC3 and ACS footprints, respectively.

to what is expected for young globular clusters, such as mass and radius. Therefore, by studying YMCs, we may be able to study the formation of today's globular clusters.

While the interiors of mergers have been well-studied in the past, few surveys have looked at the tidal debris associated with mergers. However, simulations are now showing that star formation can occur in the extended regions of a merger. Simulations with explicit stellar feedback indicate that ~ 20–50 per cent of a merger's SFR can occur in extended debris (Hopkins et al. 2013). Observations of the Tadpole galaxy confirm this prediction, as ~ 30 per cent of the system's star formation is occurring in tidal tail star clusters (Jarrett et al. 2006). Tidal tails also offer a relatively clean and uncluttered environment as compared to the interiors of galaxies. Their sparse environments mean clusters will not be subject to shocks and tides found in the dense nuclear region, and may avoid disruption, surviving to the present day (Renaud 2018).

Despite the differences in location and interaction, several common properties seem to exist between studies of YMCs found in merging and quiescent galaxies. The slopes of the mass and luminosity functions has been measured to be between -1.8 and -2.2 for both types of galaxies. The cluster formation efficiency (CFE), a measure of the percentage of the SFR occurring within star clusters, tracks the local SFR density in both environments. Additionally, cluster radii are similar, with half-light radii of ~ 0.5–10 pc (Portegies Zwart, McMillan & Gieles 2010). Such similarities suggest common physics behind star cluster formation.

This paper builds on previous work by Mullan et al. (2011) and Knierman et al. (2003), who studied clusters in tidal tails using the WFPC2 camera on *HST*. Both works found statistically significant populations of clusters in a variety of tails, with colours suggesting masses comparable to the YMCs found in the interiors of mergers. Merging systems with young interaction ages and bright tails produced the most star clusters. However, analysis was limited by the lack of multiband photometry. Our new observations of 12 tails in seven interacting systems add F336W and F438W WFC3 and F435W ACS imaging to existing WFPC2 F606W and F814W observations, to allow for age and mass determination.

We will begin in Section 2 by describing our imaging data sets and our analysis methods. In Section 3, we show our results. In

Section 4, we discuss our findings and conclude our chapter with the main points of our research in Section 5. We add notes for individual tails in Section A.

2 DATA ANALYSIS

Our analysis consists of two parts: *HST* imaging to identify tidal tail star clusters and determine their ages and masses, and UV imaging with *GALEX* and *Swift* to derive the local SFRs. Both efforts are described below.

2.1 *HST*

Our optical and near-IR observations consist of WFPC2, ACS, and WFC3 imaging from *HST* across multiple cycles; the full sample is shown in Fig. 1. Properties of our sample are highlighted in Table 1, with systems ordered according to their interaction age. We sample not only major disc mergers but also minor and dwarf mergers as well.

WFPC2 F555W and F814W data were taken in Cycle 7 (GO 7466) Knierman et al. (2003) for NGC 3256. The remaining samples of AM1054-325, MCG-03-068-13, NGC 1487, NGC 2992, NGC 2993, NGC 6872, and NGC 1614 were observed with WFPC2 in Cycle 16 (GO 11134), in F606W and F814W Mullan et al. (2011). Galaxies from Mullan et al. (2011) represent an extension of the original sample in Knierman et al. (2003), designed to sample a variety of ages, mass ratios, and optical properties. Our survey adds WFC3 F336W and WFC3 F438W/ACS F435W imaging to galaxies lying in the Southern hemisphere, which have also been observed with the Gemini-South GMOS detector, and will be the subject of a forthcoming paper on the diffuse light in the tidal debris. Archival ACS F438W and WFC3 F336W data for NGC 1614N/S are used from Cycle 14 (GO 10592) and Cycle 23 (GO 14066). A full description of our *HST* observations is in Table 2. We refer to our F606W, F814W, F336W, F438W, and F435W observations as V_{606}, I_{814}, U_{336}, B_{438}, and B_{435}, respectively.

WFPC2 data were reduced in IRAF and corrected for degraded charge transfer effects (CTE) using Dolphin (2000). We refer the reader to the respective papers (Knierman et al. 2003; Mullan et al.

Table 1. System information. Interaction age gives the most recent interaction, which produced the visible tidal features.

System	Interaction age (Myr)	Distance (Mpc)	Merger type	Tidal features	Tidal features μ_V (mag arcsec^{-1})
NGC 1614N/S	50	65.6	Major	Tidal tails	22.27/23.00
AM1054-325/ESO 376–28	85	52.9	Major	Tidal tails and tidal dwarf	22.65/22.76
NGC 2992/3	100	36.6	Major	Tidal tails and tidal bridge	23.47/24.78
MCG-03-13-063	100	46.2	Minor	Extended spiral arm	23.91
NGC 6872	150	62.6	Minor	Tidal tails	24.06
NGC 3256E/W	400	42.8	Major	Tidal tails	24.04/23.75
NGC 1487E/W	500	10.8	Dwarf	Tidal tails	24.02/24.57

Table 2. *HST* observations.

System	Filter	Exposure time (s)	Date	Program ID	Camera
NGC 1614N/S	F336*W*	6510	2015 Dec 12	14 066	WFC3
	F438W	1260	2006 Aug 14	10 592	ACS
	F606W	1900	2007 Nov 15	11 134	WFPC2
	F814W	1900	2007 Nov 15	11 134	WFPC2
AM 1054–325/ESO 376–28	F336W	3440	2017 Nov 6	14 937	WFC3
	F435W	1520	2017 Nov 7	14 937	WFC3
	F606W	1900	2008 Feb 24	11 134	WFPC2
	F814W	1900	2008 Feb 24	11 134	WFPC2
NGC 2992	F336W	2230	2018 Nov 27	15 083	WFC3
	F438W	2100	2018 Apr 19	15 083	ACS
	F606W	1000	2007 Dec 28	11 134	WFPC2
	F814W	900	2007 Dec 28	11 134	WFPC2
NGC 2993	F336W	2230	2018 Apr 19	15 083	WFC3
	F438W	2100	2018 Nov 27	15 083	ACS
	F606W	1000	2007 Dec 3	11 134	WFPC2
	F814W	900	2007 Dec 3	11 134	WFPC2
MCG-03-13-063	F336W	3420	2017 Sep 27	14 937	WFC3
	F435W	1520	2017 Sep 28	14 937	WFC3
	F606W	1000	2007 Nov 24	11 134	WFPC2
	F814W	900	2007 Nov 24	11 134	WFPC2
NGC 6872[a]	F336W	3920	2018 Jul 24	15 083	WFC3
	F435W	1760	2018 Jul 24	15 083	WFC3
	F606W	2100/1900	2008 Feb 23/2008 May 16	11 134	WFPC2
	F814W	2100/1900	2008 Feb 23/2008 May 16	11 134	WFPC2
NGC 3256E	F336W	3520	2018 Jun 15	15 083	WFC3
	F435W	1600	2018 Jun 15	15 083	WFC3
	F555W	1000	1999 Oct 11	7466	WFPC2
	F814W	1000	1999 Oct 11	7466	WFPC2
NGC 3256W	F336W	3520	2018 Jan 15	15 083	WFC3
	F435W	1600	2018 Jan 15	15 083	WFC3
	F555W	1000	1999 Mar 24	7466	WFPC2
	F814W	1000	1999 Mar 24	7466	WFPC2
NGC 1487E	F336W	3520	2017 Nov 25	15 083	WFC3
	F435W	1600	2017 Nov 25	15 083	WFC3
	F606W	1000	2008 Aug 9	11 134	WFPC2
	F814W	900	2008 Aug 9	11 134	WFPC2
NGC 1487W	F336W	3520	2019 Mar 24	15 083	WFC3
	F435W	1600	2019 Mar 24	15 083	WFC3
	F606W	1000	2008 Aug 31	11 134	WFPC2
	F814W	900	2008 Aug 31	11 134	WFPC2

[a]NGC 6872 was measured in two pointings with WFPC2.

2011) for a more in-depth discussion on WFPC2 data reduction. WFPC2 magnitudes were taken from Mullan et al. (2011) and Knierman et al. (2003). Objects in Knierman et al. (2003) were transformed from the WFPC2 Vegamag photometric system to the Johnson–Cousins system using transformations found in Holtzman et al. (1995), going from F555W and F814W to *V* and *I*. Rather than converting back to WFPC2 magnitudes, we keep them in their transformed system. Data from Mullan et al. (2011) were provided in WFPC2 Vegamag magnitudes (V_{606} and I_{814}).

ACS and WFC3 images were downloaded from the *HST* archive, which have been processed through the standard ACS and WFC3 pipelines. ACS images have a scale of 0.05 arcmin per pixel, while WFC3 observations have a scale of 0.04 arcmin per pixel. This is compared to the WFPC2 WF scale of 0.1 arcmin per pixel;

Table 3. *GALEX* and *Swift* observations.

System	Observatory	Filter	Exposure time (s)	Observation ID	Observation date
NGC 1614N/S	*Swift*	UVM2	3271.5	00046270001; 00 046 270 002	2012 May 10; 2012 Jul 6
AM1054-325/ESO 376–28	*GALEX*	FUV	108	6 386 924 688 810 967 040	2007 Feb 3
NGC 2992/3	*GALEX*	FUV	1045.5	2 485 918 962 089 459 712	2005 Feb 12
MCG-03-13-063	*GALEX*	FUV	204	6 381 260 060 739 239 936	2006 Jan 8
NGC 6872	*GALEX*	FUV	3371.3	2 505 622 210 593 423 360	2006 Jun 29
NGC 3256E/W	*Swift*	UVM2	1867.2	00049720003; 00 049 720 012	2013 Sep 15; 2014 Sep 18
NGC 1487E/W	*GALEX*	FUV	108	6 385 833 989 382 340 608	2007 Jan 5

objects on the WFPC2 PC were not analysed due to its larger readnoise.

We perform aperture photometry on all our objects using the DAOPHOT.PHOT (Stetson 1987) task in IRAF. We choose to match the aperture settings in Mullan et al. (2011), which uses radii of 2, 5, and 8 pixels for object, inner background, and outer background annuli, respectively. When translated to the WFC3 scale, this results in radii of 5, 12.5, and 20 pixels. For ACS, we use radii of 4, 10, and 16 pixels. In this manner, we are assured that we are measuring our clusters to the same physical extent, camera to camera. Aperture corrections to bright, isolated stars were performed out to a radius of 10 pixels for WFC3 and ACS imaging. Due to the lack of adequate stars in the NGC 1487 field, we take the average aperture corrections from all other fields and apply them to NGC 1487W and NGC 1487E. 10 pixel zero-points of 23.392, 24.895, and 25.762 were used for U_{336}, B_{438}, and B_{435}, respectively.

2.2 GALEX

The *Galaxy Evolution Explorer* (*GALEX*) operated from 2003 to 2012 as an orbiting UV telescope. Its 50 cm diameter mirror imaged a $1.25°$ FOV with two separate microchannel-plate detectors, designated as the near-ultraviolet (NUV) and far-ultraviolet (FUV) channels. The telescope has a pixel scale of 1.5 arcmin per pixel. *GALEX* conducted several surveys, including the All-Sky Imaging survey (AIS), Medium Imaging Survey (MIS), Deep Imaging Survey (DIS), and Nearby Galaxy Survey (NGS), to varying depths. Our targets are drawn from AIS (AM1054-325, ESO 376–28, MGC-03-13-063, NGC 1487E/W) and NGS (NGC 6872, NGC 2992, NGC 2993). Our *GALEX* observations are listed in Table 3, along with our *Swift* observations (described below).

We use images taken in the FUV ($\lambda_{eff} = 1538.6$ Å) obtained from the MAST archive. These have been pipeline processed. While background subtracted images are available via MAST, we do not use these because the background subtraction can be inaccurate for extended objects. Photometry was performed on the entire flux enclosed within the tail boundary, as described in Section 2.4. The sky background was determined by sampling five nearby regions of 30 x 30 pixels and taking the mean value. For NGC 2992, a bright, blue star visible in the FUV image was manually masked.

We corrected for Galactic extinction using coefficients from Yuan, Liu & Xiang (2013) for *GALEX* FUV.

2.3 Swift

NGC 3256 and NGC 1614 do not have FUV exposures with *GALEX*; instead, we have opted to use NUV data from *Swift*, downloaded from the MAST archive. The *Swift* satellite operates the 30 cm UltraViolet-Optical Telescope (UVOT), with a FOV of 17 x 17 arcmin. Images were taken in 2×2 binned mode, with a pixel scale of 1 arcmin

per pixel. The UVOT CCD operates as a photon counter, which is susceptible to coincidence loss if two or more photons arrive within a single frame. The effect of this scales with brightness, and past analysis has shown that coincidence loss becomes greater than 1 per cent when the count rate is greater than 0.007 counts s^{-1} pixel^{-1}; for 2 x 2 binned images, as we use, the count rate threshold is then 0.028 counts s^{-1} pixel^{-1}. The faint tails of these two systems, NGC 3256 and NGC 1614, fall well below this threshold, and we can discount effects from coincidence loss.

Swift offers three UV filters, *uvw1*, *uvw2*, and *uvm2*. We use the *uvm2* filter ($\lambda_{eff} = 2221$Å) as the other two filters have extended red tails which leak optical light into the UV. Images were co-added together using the HEASOFT software package.

Photometry was performed using the previously mentioned procedure for *GALEX* imaging. Extinction coefficients were taken from Roming et al. (2009) for the *uvm2* filter.

2.4 Tail definition

Regions defined as tidal debris are taken from Mullan et al. (2011). The 'in-tail' and 'out-of-tail' regions were defined using images taken with the WFPC2 V_{606} filter. Images were smoothed with a Gaussian kernel at 5–7 pixels full width at half-maximum (FWHM), and a contiguous region one count above background was defined as 'in-tail', using SAO DS9; all other regions were defined as 'out-of-tail'. In the cases of NGC 1487W, AM1054-325, ESO 376–28, and NGC 6872, the centre of the galaxy is imaged as well. The boundary between the centre and the tail is found where the radial light profile changes in scale length.

2.5 Cluster detection

Objects were detected using the DAOPHOT.DAOFIND (Stetson 1987) task in IRAF. Selection criteria for the initial WFPC2 cluster list required 2 counts per object in both V_{606} and I_{814}, a signal-to-noise ratio (S/N) of at least 3, error in F606W less than 0.25 mag, and detections in at least one dither position. For our ACS/WFC3 imaging, we require an S/N of at least 3 in both U_{336} and B_{438}/B_{435}. Objects had to be detected in all four filters. We further excluded objects that were fit to our simple stellar population (SSP) cluster models (Marigo et al. 2008) with a $\chi^2 > 3$.

Magnitude and colour cuts were applied to our source catalogue to separate potential clusters from contaminant stars and background galaxies. Objects that met these requirements are defined as star cluster candidates (SCCs). We apply a magnitude cut of $M_V < -8.5$ ($M_{F606W} < -8.6$) designed to eliminate individual stars. Magnitude cuts between $-8 < M_V < -9$ are commonly used in studies of star clusters (Konstantopoulos et al. 2010). Whitmore et al. (2010) found that even at fainter magnitudes, down to $M_V = -7$, more than 60 per cent of detected objects were clusters as opposed to individual
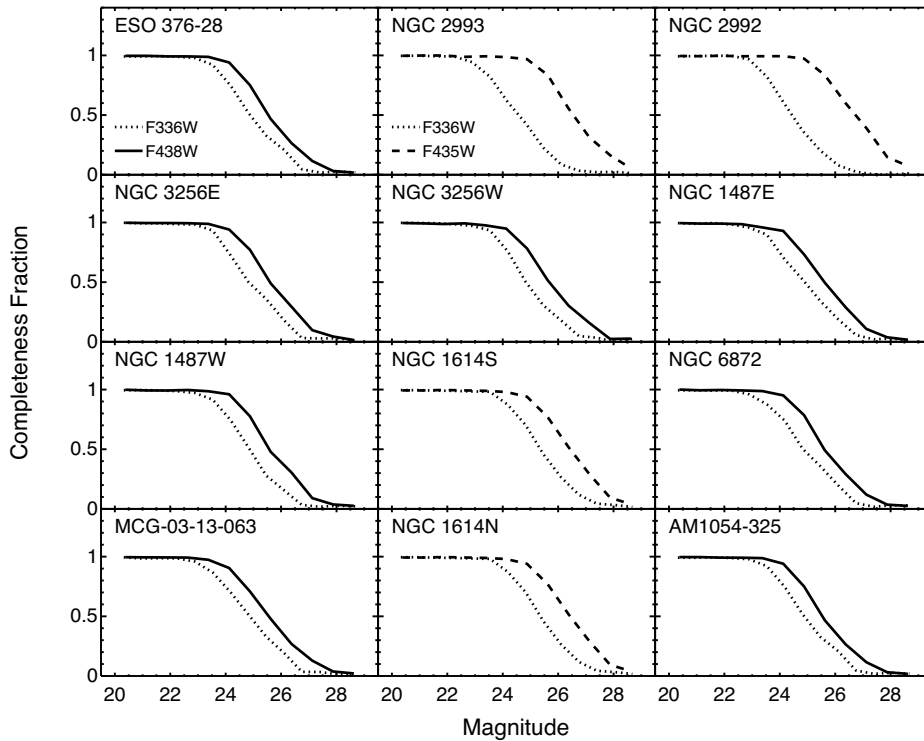
Figure 2. Completeness data for our WFC3 F336W/F435W and ACS F438W imaging. Solid curves represent data for F438W, dotted curves represent data for F336W, and dashed curves represent data for F435W.

stars, adding confidence to our selection criteria. In addition to discriminating against non-clusters, a magnitude cut allows a uniform measurement standard across our systems, most of which have nearly complete samples of SCCs down to the $M_V = -8.5$ cut-off, as shown in Section 2.6. A colour cut of $V - I < 2.0$ ($V_{606} - I_{814} < 1.4$) is added as well; this will still allow for old globular clusters that have reddened as they evolve, while eliminating individual stars.

2.6 Completeness

Completeness curves from Mullan et al. (2011) show that our WFPC2 data are on average 50 per cent complete at $m_{V_{606}} \approx 25.5$ and $m_{I_{814}} \approx 24.5$. To measure the completeness of our WFC3 and ACS imaging, we perform a similar analysis as in Mullan et al. (2011); we add 10 000 fake stars to each individual image, 100 at a time, with DAOPHOT.ADDSTAR (Stetson 1987), and calculate how many are recovered above a 3σ limit. Our completeness curves are shown in Fig. 2. For systems AM1054-325, ESO 376–28, NGC 3256, NGC 1487, MCG-03-13-063, and NGC 6872, we are complete at 50 per cent at $m_{B_{438}} = 25.5$ and $m_{U_{336}} = 24.8$. NGC 2992 and NGC 2993 are 50 per cent complete at $m_{B_{435}} = 26.5$ and $m_{U_{336}} = 24.5$. NGC 1614, observed with programme GO-14066 and GO-10592 is complete at $m_{B_{435}} = 26.5$ and $m_{U_{336}} = 25.4$.

3 RESULTS

3.1 Colour–colour diagrams

In Figs 3–14, we show the $U_{336} - B_{438}$ versus $V_{606} - I_{814}$ colour–colour diagrams for all our observed systems. Systems are ordered in reference to the age of the tidal debris (see Table 1). The interaction age of the merger is plotted as a yellow circle. Objects that fulfill

our SCC criteria in Section 2.5 are shown as dark blue circles. For completeness, we show objects that do not meet our criteria as grey boxes, with arrows indicating upper and lower limits.

Data are plotted against SSP models from Marigo et al. (2008), with logarithmic ages overplotted on the evolutionary track. We use a Salpeter IMF; however, the choice of IMF is negligible in determining ages, and the tracks are also consistent expectations for a Chabrier (Chabrier 2001) or Kroupa (Kroupa 2001) IMF. We corrected for foreground Galactic extinction using an $R_\lambda = A_\lambda/E(B - V)$ reddening law, with $R_V = 3.1$, with data from Schlafly & Finkbeiner (2011). Internal cluster extinction is not corrected for when plotting our colour–colour diagrams. However, this is taken into account when spectral energy distribution (SED) fitting our clusters (Section 3.3). We also include a reddening arrow in the lower right hand corner of our plots for $A_V = 0.5$.

The area inside and outside the tail was calculated using SAO DS9 regions of the tail, as defined in Section 2.4. We subtract the cluster density outside the tail ($N_{\text{out}}^{\text{SCC}}/A_{\text{out}}$) from inside the tail ($N_{\text{in}}^{\text{SCC}}/A_{\text{in}}$) to determine the excess cluster density, Σ_{SCC}. Errors are determined from Poisson statistics. Half of our tails show excesses above the 3σ level, indicating significant amounts of SCCs. It is important to note that while some systems may not contain significant numbers of SCCs, some individual objects in tails may still be real star clusters. The data are shown in Table 4.

We perform Kolmogorov–Smirnov (KS) tests on the distributions of $U_{336} - B_{438}$, $B_{438} - V_{606}$, and $V_{606} - I_{814}$ colours between in-tail and out-of-tail objects for all detected objects and for SCCs only. This is another way to determine the likelihood that objects within the tail are unique and independent from those outside the tail region, in addition to measuring cluster excess. Recorded p-values are shown in Table 5. Our $V_{606} - I_{814}$ colour is most useful in discriminating between tail and non-tail objects. Of the eight systems which contain
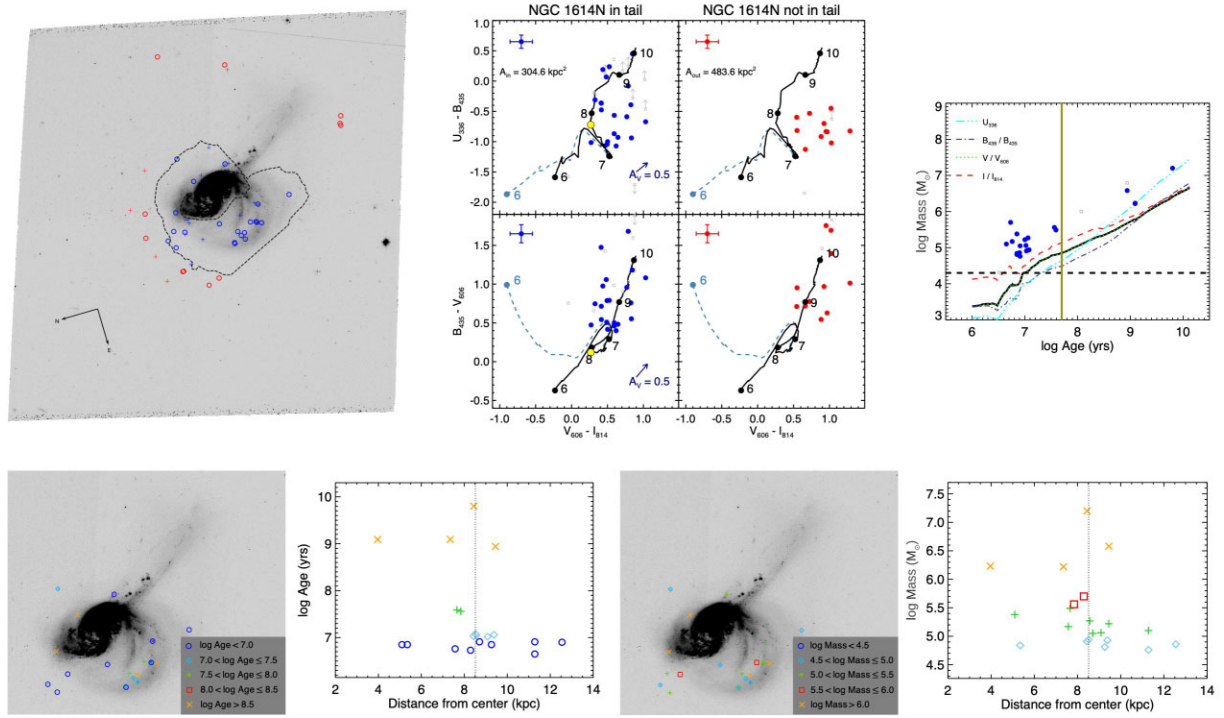
Figure 3. *Top left*: *HST B_{435}*-band image of NGC 1614N, with the tail region outlined with a black, dashed curve. In-tail SCCs are shown as blue circles, while out-of-tail SCCs are red circles. Non-SCC detected objects are shown as crosses. *Top middle*: Colour–colour diagrams for in-tail and out-of-tail sources plotted against stellar evolutionary tracks from Marigo et al. (2008) in solid black; the dashed light blue line is the same track with nebular continuum and emission lines added. The yellow circle indicates the age of the merger. Blue/red circles represent SCCs for in-tail/out-of-tail sources, and grey boxes are non-SCC detected objects. The total area enclosed in each in-tail or out-of-tail region in kpc^2 is indicated on the upper left, along with median error bars. *Top right*: Ages and masses for detected objects. SCCs are shown in blue, non-SCCs in grey. The solid black curve is our magnitude limit of $M_V = -8.5$, while the red, green, purple, and cyan curves show 50 per cent completeness limits. The vertical yellow line marks the interaction age of the system, and the horizontal dashed line marks our mass cut-off of log Mass = 4.3 for our CFE determinations. *Bottom row*: Age and mass distributions for our SCCs. A vertical dashed line marks the median distance from the centre. We find 21 in-tail SCCs, and 11 out-of-tail SCCs for NGC 1614N. The tail curls to the north from the east, with young clusters scattered throughout the region.

enough SCCs for a KS test, five of them show *p*-values less than 0.04, indicating the data are drawn from independent distributions.

3.2 Addition of nebular flux

Clusters less than 10 Myr old can show strong emission lines, as the surrounding hydrogen gas from cluster formation is ionized and undergoes recombination. An example of these systems is shown in Fig. 15 for NGC 1614. As clusters will expel their hydrogen gas via stellar feedback on time-scales of several million years (Pang et al. 2020), the presence of recombination lines indicates recent star formation.

Our SSP model (the black solid line in Figs 14 and 3 does not contain nebular continuum emission, nor flux from emission lines; we use Starburst99 (Leitherer et al. 1999) to calculate contributions from the nebular continuum, as well as the H α and H β emission lines. We include the H γ line, with the flux ratio of H γ/H $\beta = 0.47$ (Osterbrock 1989), and the O III and O II lines as well. The oxygen lines are determined from the KPNO International Spectroscopic Survey (KISS) sample of nearby, low-mass star-forming galaxies (Salzer et al. 2005); we take the median log ratio of these lines to the H β line, O III/H $\beta = 0.08$ and O II/H $\beta = 0.56$.

The effect of the emission lines depends on the filter. The H α, H β, and O III lines are covered by the F606W filter, while the H γ

line falls in the middle of the B_{438} and B_{435} filters. The O II line is at the edge of the F435W and F336W filters. The result is that the V_{606} filter is most strongly affected by the presence of emission lines, due to the strong H α and H β lines, while the effect in the other filters is relatively inconsequential. This shifts the V_{606}–I_{814} colour towards bluer colours in our colour–colour plots. The resulting evolutionary track is degenerate with extinction for ages <10 Myr for our U_{336} – B_{438} versus V_{606} – I_{814} diagrams. The effect is more apparent when we plot B_{438} – V_{606} versus V_{606} – I_{814}; the evolutionary track dramatically swings upwards in our plots as the B_{438} – V_{606} colour trends towards redder values. This effect is seen for similar young clusters in interacting systems as well, using the V_{606} filter (Gallagher et al. 2010; Fedotov et al. 2011, 2015).

Data for NGC 3256 were taken from Knierman et al. (2003). For NGC 3256W/E, we determined the magnitudes in the F555W and F814 filters, and then transformed these to the Johnsons–Cousins system, as in Knierman et al. (2003), using transformations from Holtzman et al. (1995). The shape and wavelength boundaries of the F555W filter transmission are noticeably different from the V_{606} filter in that the H α line falls at the edge of the filter, thus it has a much less of an effect on our model magnitudes. Therefore, on the colour–colour diagrams for NGC 3256W/E, there is less of a difference between the nebular emission evolutionary tracks and the SSP models than for our other systems.
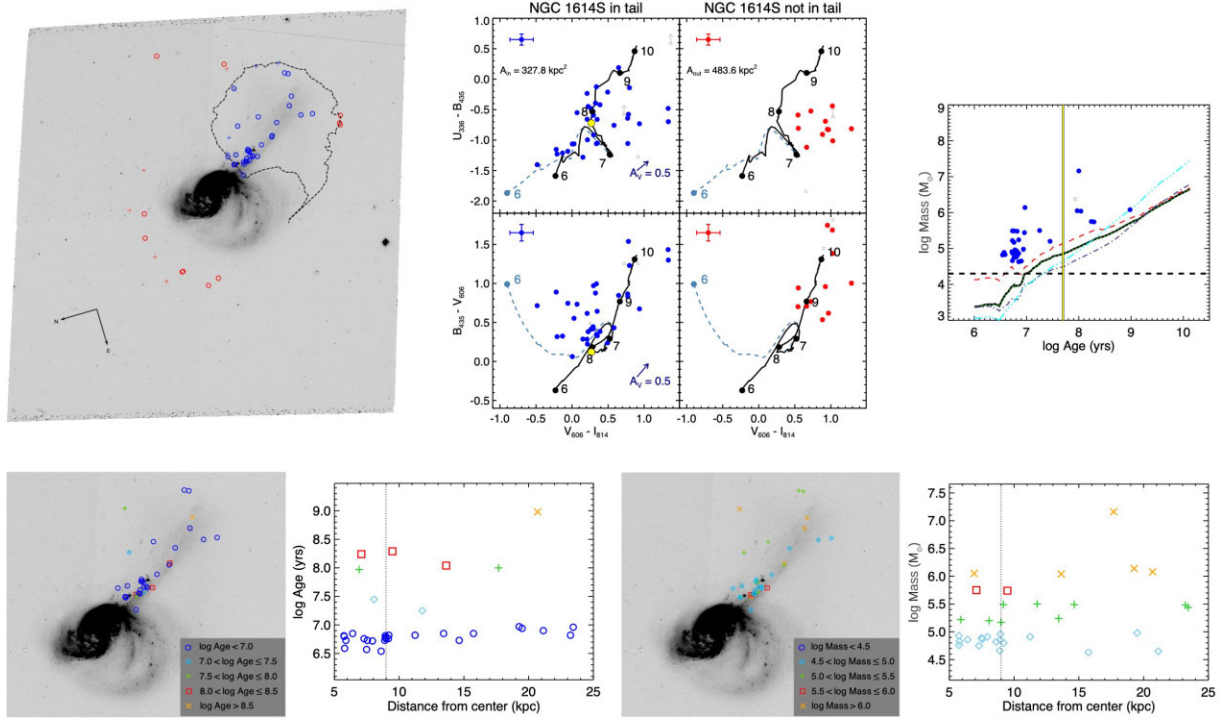
Figure 4. Same as Fig. 3, but for NGC 1614S. We find 33 in-tail SCCs, and 11 out-of-tail SCCs. This system has a statistically significant excess cluster density above 3σ. The tail extends to the south from the centre of the merging system. Young objects are found throughout the tail, similar to NGC 1614N.
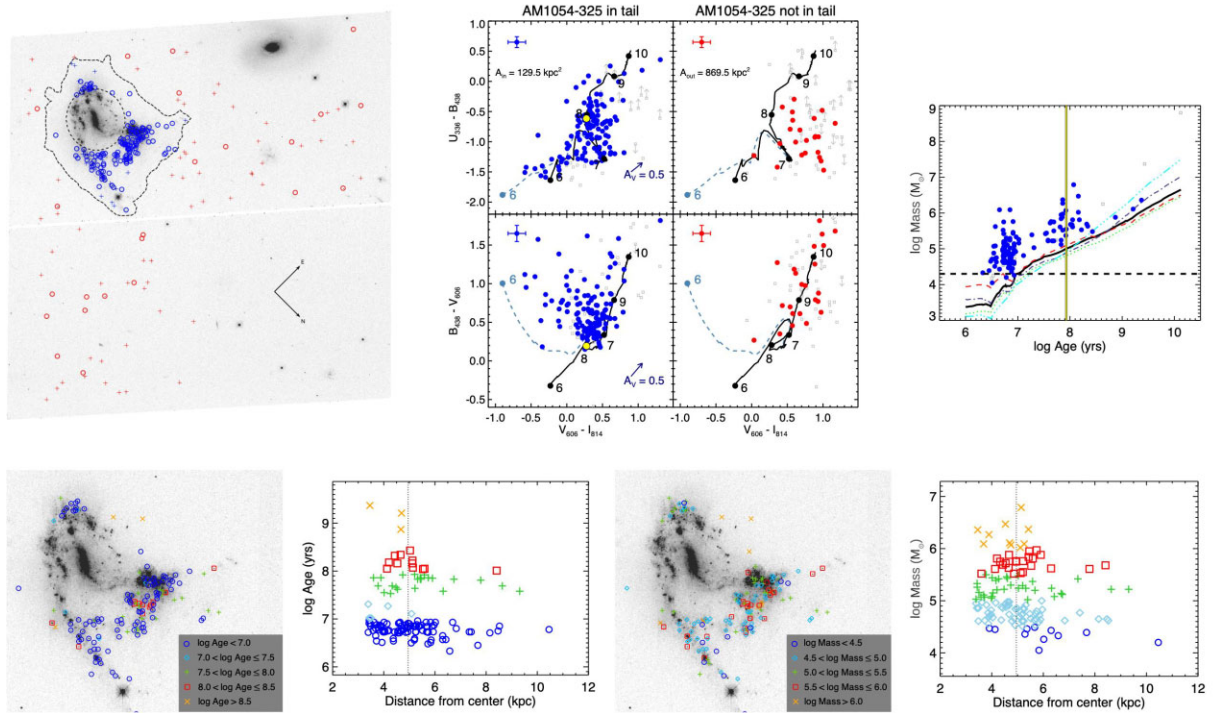

Figure 5. Same as Fig. 3, but for AM1054-325. We find 135 in-tail SCCs, and 23 out-of-tail SCCs. This system has a statistically significant excess cluster density above 3σ. A tidal dwarf is directly north of the centre of the galaxy, while the tidal tail extends northwards from the western edge. Many SCCs show signs of emission lines, indicated by their large $B - V$ values. Its interacting partner can be seen at the top right of the image.
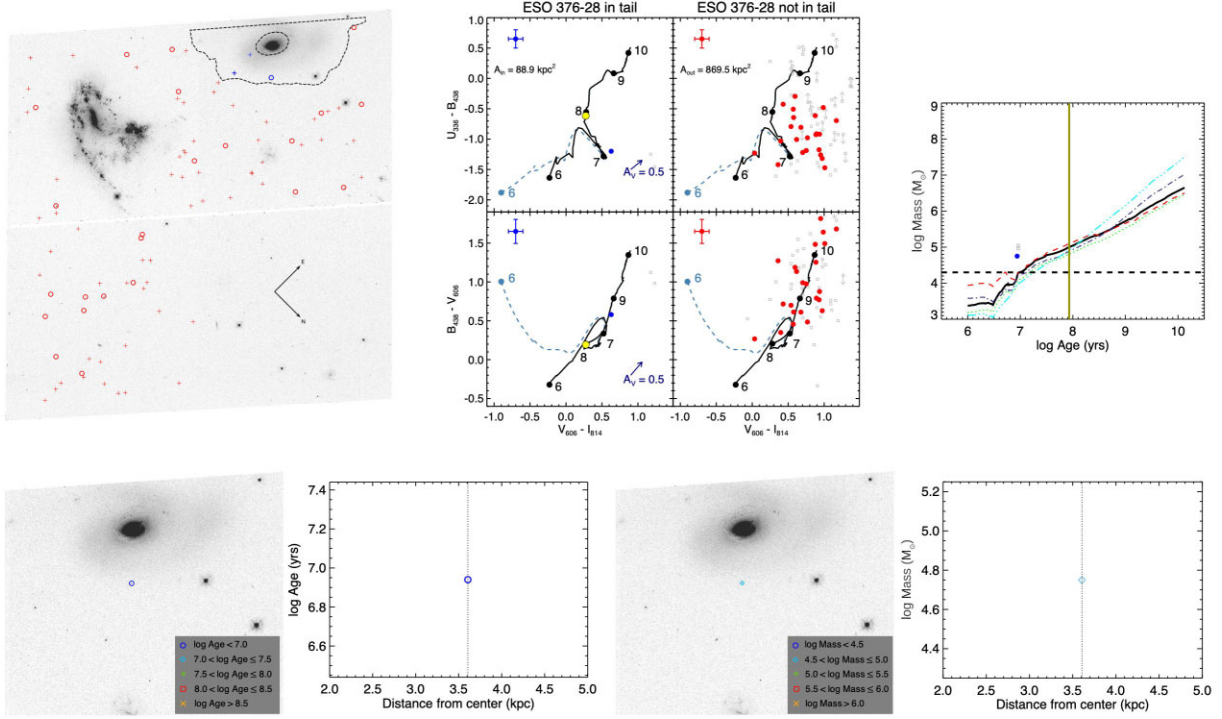
Figure 6. Same as Fig. 3, but for ESO 376–28. We find 1 in-tail SCC, and 23 out-of-tail SCCs. Little structure is seen in this galaxy.
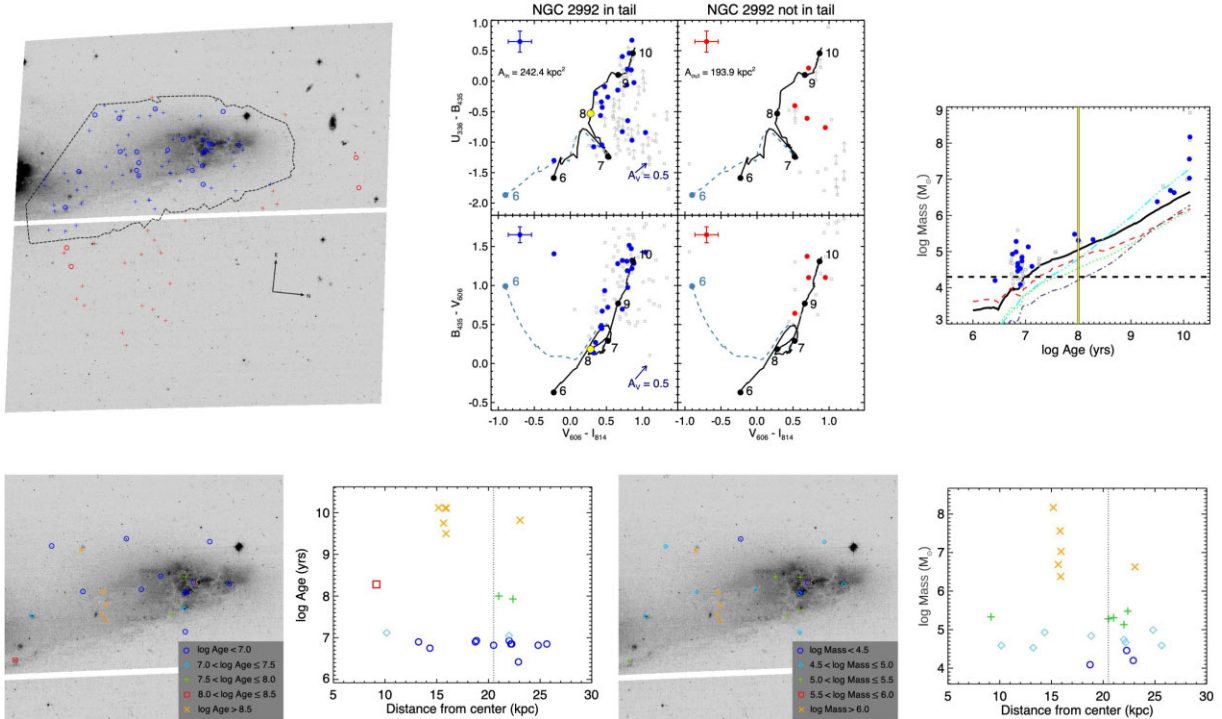
Figure 7. Same as Fig. 3, but for NGC 2992. We find 22 in-tail SCCs, and 4 out-of-tail SCCs. This system has a statistically significant excess cluster density above 3σ. We have targeted the tidal dwarf, with the northern edge of the galaxy NGC 2992 shown on the left. We do not include sources from the galaxy itself.

3.3 Ages and masses

Ages and masses of clusters were determined using the 3DEF SED fitting code, as described in Bik et al. (2003). This code compares a set of input magnitudes to a grid of SSP models with ages between 10^6 and $10^{10.12}$ yr. It will apply an extinction to our observed magnitudes through a range of $E(B - V)$ values, compare the set of model magnitudes and extincted, observed magnitudes, and minimize the resulting χ^2 value to determine the best-fitting
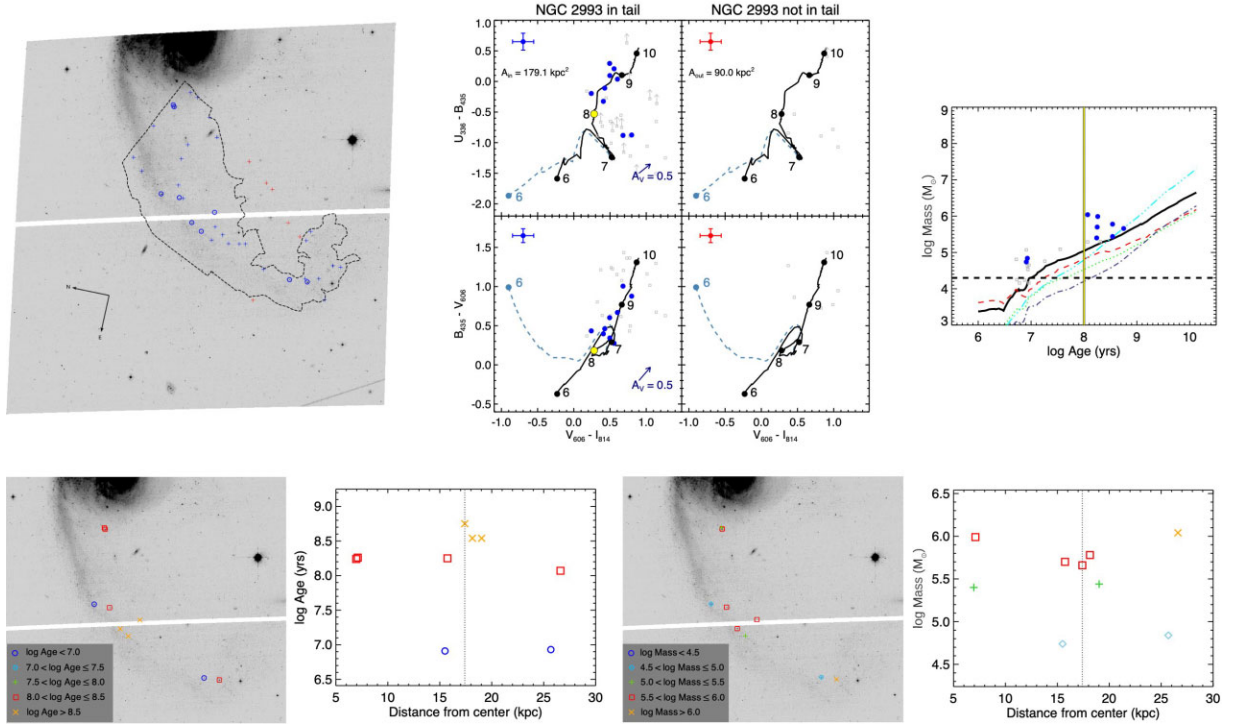
Figure 8. Same as Fig. 3, but for NGC 2993. We find 9 in-tail SCCs, and 0 out-of-tail SCCs. We capture the tidal tail of NGC 2993 (seen at the top of the image). Most of the SCCs in the tail have ages comparable to the interaction age of the NGC 2992/3 system.
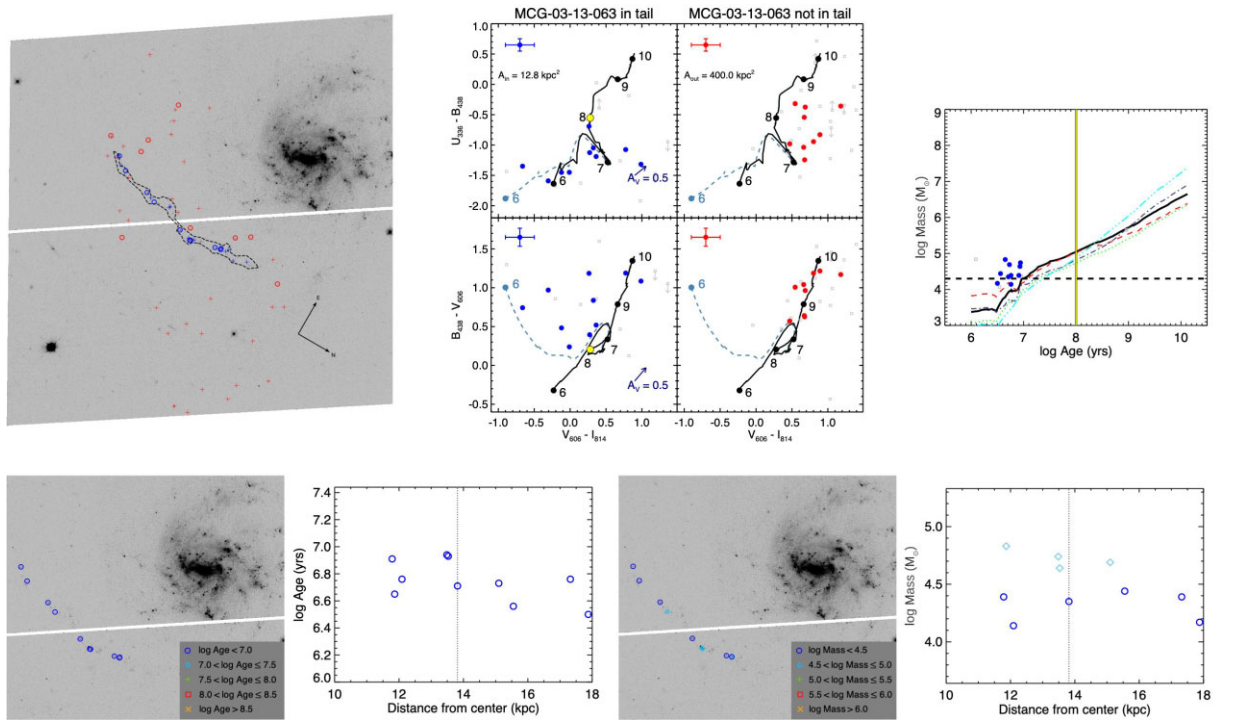

Figure 9. Same as Fig. 3, but for MCG-03-13-063. We find 10 in-tail SCCs, and 9 out-of-tail SCCs. This system has a statistically significant excess cluster density above 3σ. An extended, thin tail is seen, produced from an unseen companion. All the SCCs in the tail are < 10 Myr.

ages and masses. We use an evolutionary track from Marigo et al. (2008) with solar metallicity and a Salpeter IMF (Salpeter 1955), with nebular flux added to it (see Section 3.2). Our models do not account for binary star evolution. Spectroscopic observations of clusters and

merging systems have found metallicities in the range of ∼1.0–1.5 $Z_{\odot}$ (Trancho et al. 2007a, b; Bastian et al. 2009b; Trancho et al. 2012; Rosa et al. 2014). For comparison, we run our 3DEF algorithm for NGC 6872, with 158 SCCs, using a tracks at 0.5 $Z_{\odot}$ and 2 $Z_{\odot}$. We
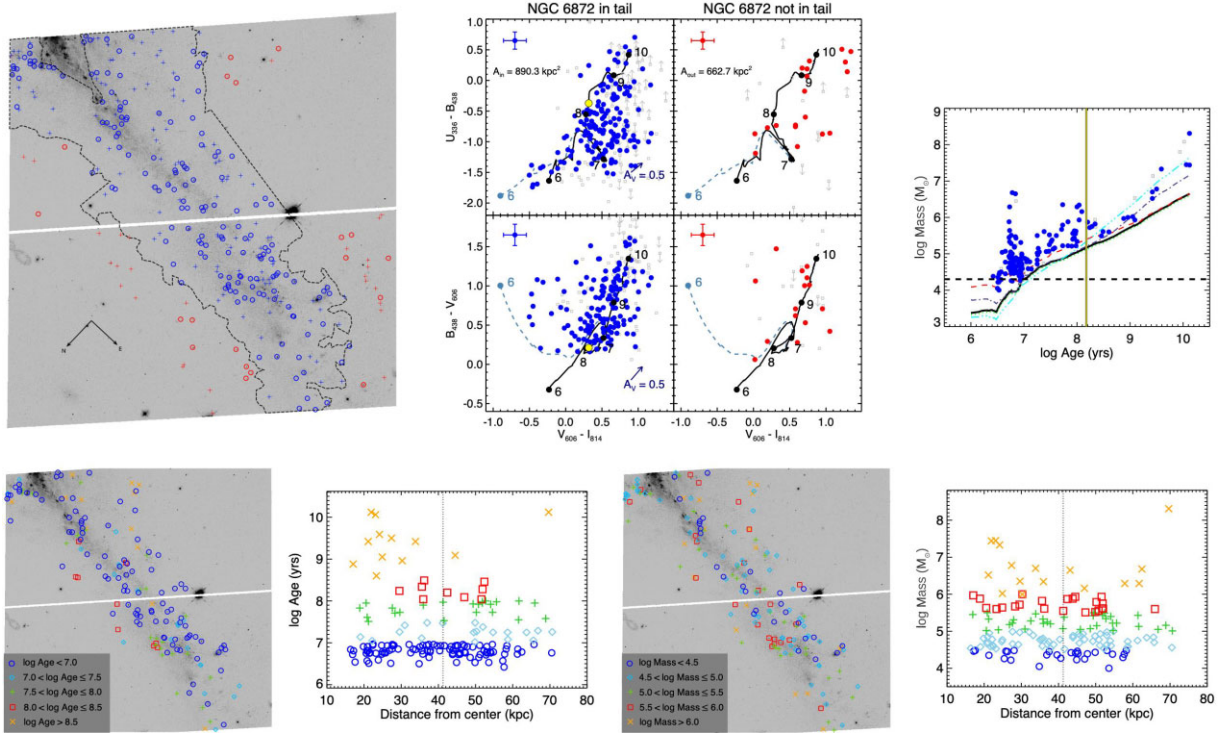
Figure 10. Same as Fig. 3, but for NGC 6872. We find 158 in-tail SCCs, and 19 out-of-tail SCCs. This system has a statistically significant excess cluster density above 3σ. This is Eastern tidal tail of NGC 6872, which stretches out to 70 kpc; the centre of the galaxy lies to the west. A range of ages are seen, with young SCCs spread out along the length of the tail.
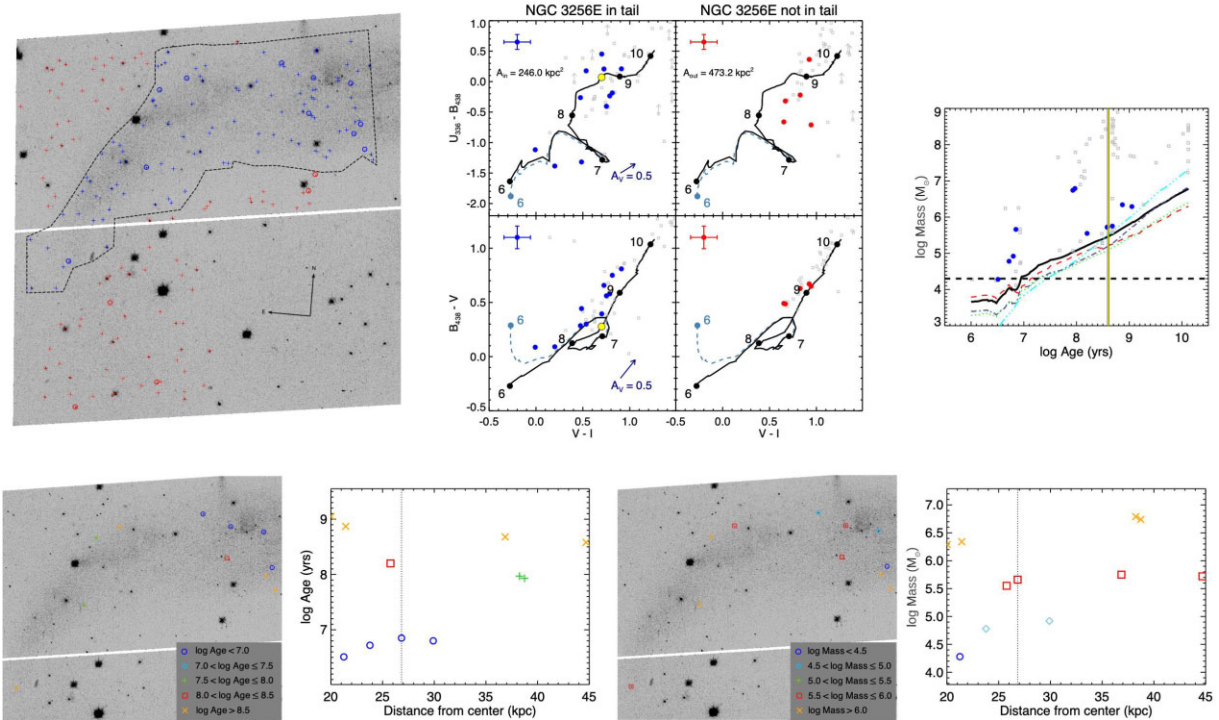

Figure 11. Same as Fig. 3, but for NGC 3256E. We find 11 in-tail SCCs, and 5 out-of-tail SCCs. Emission-line clusters do not clearly stand out, as the NGC 3256 system was imaged with the F555W filter, which weakly covers the H α line. Despite the old age of the interaction, we see a few SCCs with young ages.
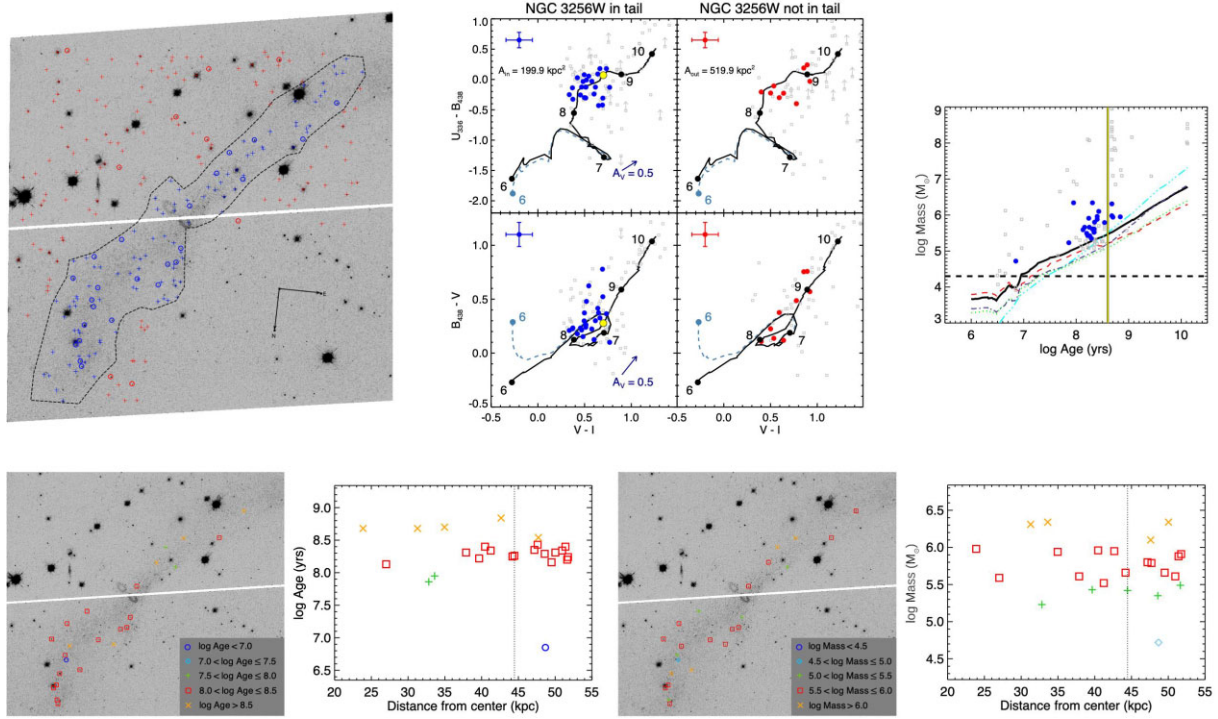
Figure 12. Same as Fig. 3, but for NGC 3256W. We find 24 in-tail SCCs, and 9 out-of-tail SCCs. This system has a statistically significant excess cluster density above 3σ. Many of the SCCs are clustered around the interaction age of the merger, suggesting they formed from the interaction.
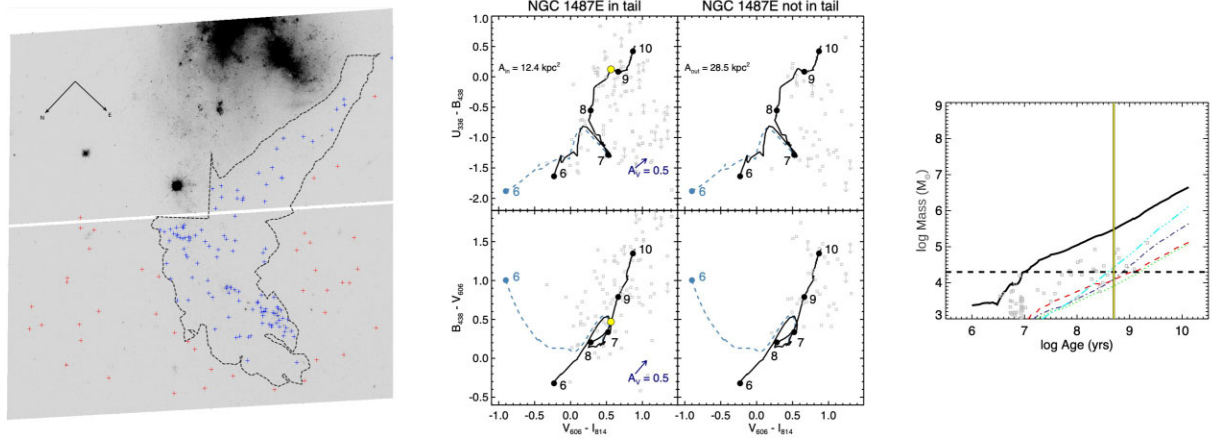

Figure 13. Same as Fig. 3, but for NGC 1487E. We find 0 in-tail SCCs, and 0 out-of-tail SCCs. Note that as NGC 1487E has no detected SCCs, age and mass distribution figures are not included. Although no SCCs are found in this system, a large number of non-SCC objects are detected, which do not make the $M_V < -8.6$ cut-off. This suggests the presence of low-luminosity, low-mass objects.

find the median ratio of ages and masses determined using solar and half solar metallicity to be 1 and 1.1, respectively. The ratio of ages and masses between $Z_\odot$ and $2\,Z_\odot$ is 1.02 and 0.98, respectively. A comparison of the different metallicities and their effects on our $U_{336}-B_{438}$, $B_{438}-V_{606}$, and $V_{606}-I_{814}$ colours is shown in Fig. 16. Here, we plot data for NGC 6872 against SSP models and SSP models with nebular emission added, for metallicities of $Z_\odot$, $0.5\,Z_\odot$, and $2\,Z_\odot$. The similarity between all three metallicities shows that our age and mass estimates will not be sensitive to our chosen metallicity.

The choice of IMF will influence the masses of our clusters, but generally has little effect on the derived ages. A Chabrier or Kroupa

IMF will decrease the masses by a factor of ~ 2 relative to our assumed Salpeter IMF.

Ages and masses for all our systems are plotted individually in Figs 3–14, and collectively in Fig. 17. We see a gap in age from log Age = 7.0–7.5 yr in many of our systems; this is an artefact of the fitting process and is seen in similar studies of star clusters (e.g. Bastian et al. 2005b; de Grijs et al. 2013; Randriamanakoto et al. 2019). The true ages are likely spread over neighbouring ages. It is worth noting, however, that every system, with the exception of NGC 1487, contains SCCs with ages < 10 Myr. This shows us that tidal debris are capable of supporting cluster formation.
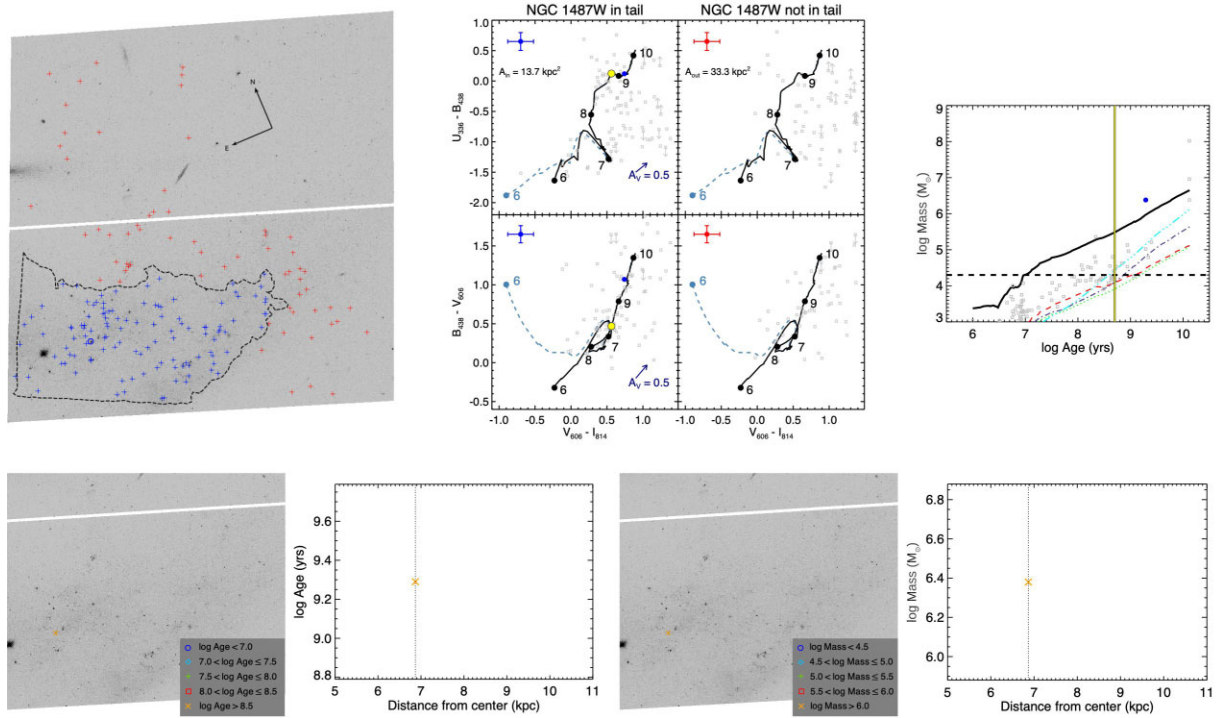
Figure 14. Same as Fig. 3, but for NGC 1487W. We find 1 in-tail SCC, and 0 out-of-tail SCCs. Like NGC 1487E, we again find a number of non-SCC objects in the tail, suggesting low-mass objects present in the tail.

Table 4. Cluster excesses.

System	$N_{\mathrm{in}}^{\mathrm{SCC}}$	$N_{\mathrm{out}}^{\mathrm{SCC}}$	A_{in} (kpc^2)	A_{out} (kpc^2)	Density$_{\mathrm{in}}$ (kpc^{-2})	Density$_{\mathrm{out}}$ (kpc^{-2})	Σ_{SCC} (kpc^{-2})
NGC 1614N	21	11	304.6	483.6	0.069	0.023	0.046 ± 0.017
NGC 1614S	33	11	327.8	483.6	0.101	0.023	0.078 ± 0.019^a
AM1054-325	135	23	129.5	869.5	1.042	0.026	1.016 ± 0.090^a
ESO 376–28	1	23	88.9	869.5	0.011	0.026	-0.015 ± 0.013
NGC 2992	22	4	242.4	193.9	0.091	0.021	0.070 ± 0.022^a
NGC 2993	9	0	179.1	90.0	0.050	0	0.050 ± 0.017
MCG-03-13-063	10	9	12.8	400.0	0.781	0.023	0.76 ± 0.25^a
NGC 6872	158	19	890.3	662.7	0.179	0.029	0.150 ± 0.016^a
NGC 3256E	11	5	246.0	473.2	0.045	0.011	0.034 ± 0.014
NGC 3256W	24	9	199.9	519.9	0.120	0.017	0.103 ± 0.025^a
NGC 1487E	0	0	12.4	28.5	0	0	0
NGC 1487W	1	0	13.7	33.3	0.073	0	0.073 ± 0.073

^{a}Signifies excess at 3σ or above.

3.4 Cluster radii

The radii of our SCCs were found using the program ISHAPE (Larsen 1999). ISHAPE requires that sources are isolated to prevent PSF blending and at a high S/N. We perform an additional cut on our SCCs by visually selecting objects that are not in crowded regions and do not have highly elliptical shapes, which could indicate we are looking at blended clusters. We choose objects with an S/N > 25 as determined by ISHAPE, as the programme also requires bright objects to perform accurate measurements.

ISHAPE will deconvolve selected sources with a user supplied PSF and a selected analytic model. Both an EFF (Elson, Fall & Freeman 1987) and King (King 1962) model have been used in the past to study star clusters. We use a King model as it has been used to describe extragalactic and Galactic globular clusters (Bastian et al. 2012;

Chandar et al. 2016; Correnti et al. 2021; Larsen, Romanowsky & Brodie 2021). ISHAPE will fit the model to an ellipse and produce the FWHM of the major axis, and the ratio between the minor and major axes (q), for each selected source. We take the FWHM as the average between the major and minor axes of the fit. We require that $q > 0.3$ to eliminate unrealistically elliptical sources, as in Brown & Gnedin (2021). ISHAPE is able to reliably determine an FWHM for sources at 10 per cent of the size of the PSF, which for our WFC3 and ACS images, corresponds to $\approx$0.2 pix (the pixel scale for WFC3 is 0.04 arcmin per pixel, and 0.05 arcmin per pixel for ACS). We remove objects smaller than this size. The result of our selection criteria reduces the number of SCCs for analysis from 425 to 57, largely as a result of selecting isolated clusters. Our furthest systems, NGC 6872 in particular, are susceptible to crowding as the angular separation for nearby objects decreases, and this is borne out in our

Table 5. KS test results for our photometric data. We include results for all of our sources on the left, and SCC objects only on the right.

| System			All					SCC only		
	N_{in}	N_{out}	KS_{U-B}	KS_{B-V}	KS_{V-I}	N_{in}	N_{out}	KS_{U-B}	KS_{B-V}	KS_{V-I}
NGC1614N	26	14	0.025	0.020	6.6×10^{-3}	21	11	0.17	0.19	7.2×10^{-3}
NGC1614S	40	14	0.068	2.0×10^{-3}	5.852×10^{-5}	33	11	0.65	0.045	1.2×10^{-4}
AM1054-325	172	51	0.40	6.9×10^{-6}	6.6×10^{-18}	135	23	0.166	4.5×10^{-3}	2.0×10^{-8}
ESO376-28	3	51	N/A	N/A	N/A	1	23	N/A	N/A	N/A
NGC2992	61	15	0.058	0.42	0.75	22	4	0.73	0.87	0.50
NGC2993	23	5	0.19	0.018	0.34	9	0	N/A	N/A	N/A
MCG-03-13-063	19	24	2.3×10^{-3}	0.73	1.8×10^{-3}	10	9	2.1×10^{-3}	0.35	1.7×10^{-3}
NGC6872	205	29	1.6×10^{-3}	0.031	0.012	158	19	0.026	0.049	0.025
NGC3256E	71	53	0.74	0.021	0.061	11	5	0.92	0.17	0.23
NGC3256W	92	74	0.055	8.1×10^{-3}	6.7×10^{-4}	24	9	0.97	0.33	0.18
NGC1487E	83	33	0.75	0.083	4.5×10^{-3}	0	0	N/A	N/A	N/A
NGC1487W	92	44	0.39	0.36	0.46	1	0	N/A	N/A	N/A

Figure 15. Colour image of NGC 1614S. The data through filters F435W (ACS), F606W (WFPC2), F814 (ACS), and F665N (ACS) were stretched with a logarithm and bias/contrast adjustment in CARTA[a]. Subsequently in GIMP[b] they were assigned the colours blue, yellow-green, red, and pink, respectively, and using a layering schema blended with the screen algorithm (English 2017). Several regions containing SCCs with emission lines are highlighted in yellow, showing that star cluster formation is ongoing in this tidal tail.

[a]CARTA: Cube Analysis and Rendering Tool for Astronomy, https://cartavis.org. [b]Gnu Image Manipulation Program, https://www.gimp.org.

reduced number of sources. As a result, we emphasize that our radii sample is biased towards isolated, physically large SCCs.

This FWHM value is converted to a half-light radius r_h (also referred to as the effective radius R_{eff}) by multiplying the FWHM by 1.48, as noted in the ISHAPE manual. We note that while an EFF and King model will produce unique FWHM values, the resulting half-light radii are similar to one another (Larsen 1999). The minimum value of r_h we are able to detect, when combining our FWHM and axis ratio limits and converting FWHM to r_h, is 0.19 pix, corresponding to 0.0076 arcmin for WFC3 and 0.0095 arcmin for ACS. We use our B_{438}- and B_{435}-band images to derive radii as they offer a better S/N than our U_{336}-band images.

Our cluster radii are shown in Fig. 18, with interacting pairs grouped together. The minimum detectable radius for each system is shown as a vertical dashed line. The combined distribution for all our sources is shown as the bottom left plot. The distribution shows
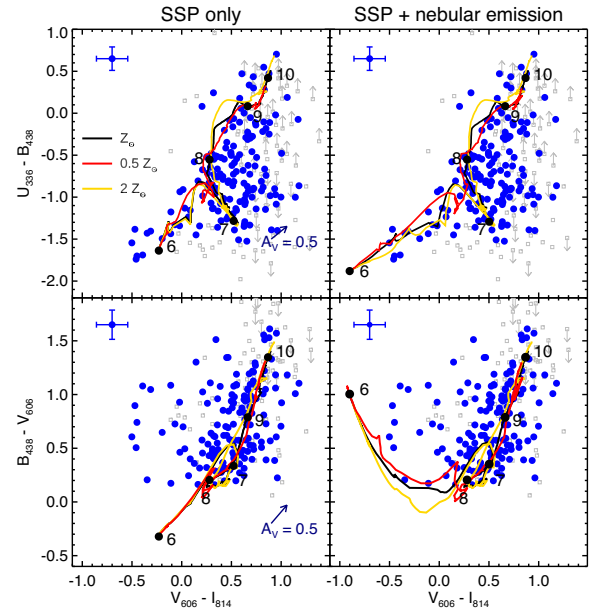
Figure 16. Comparison of SSP tracks at different metallicities, plotted against data for NGC 6872. Data points are objects that fall within the tail, as in Fig. 10. Black lines correspond to $Z = Z_{\odot}$, red corresponds to $Z = 0.5\ Z_{\odot}$, and gold corresponds to $Z = 2\ Z_{\odot}$. On the left, we plot tracks from Marigo et al. (2008). On the right, we include nebular emission (see Section 3.2) from Starburst99 models (Leitherer et al. 1999); the inclusion of line emission affects only ages < 10 Myr. In both cases, for a pure SSP and one with nebular emission added to it, the tracks are similar to one another; consequently, the ages and masses derived using either metallicity will be similar.

a peak at ≈ 5.6 pc, with an extended tail up to > 100 pc. Objects at the tail end of the distribution are likely blended together, but are included for completeness. While our objects peak at a larger value than typical of Milky Way globular clusters ($\sim$3.2 pc, Baumgardt & Hilker 2018), objects of this size are seen in both the Milky Way and in extragalactic systems (Chandar et al. 2016; Ryon et al. 2017; Baumgardt & Hilker 2018).

Note that ESO 376–28 is not included as it only contained one SCC, which was eliminated due to a low S/N in ISHAPE, and NGC 1487W's single SCC did not have a good fit. We address NGC 1487 in Section 4.6.
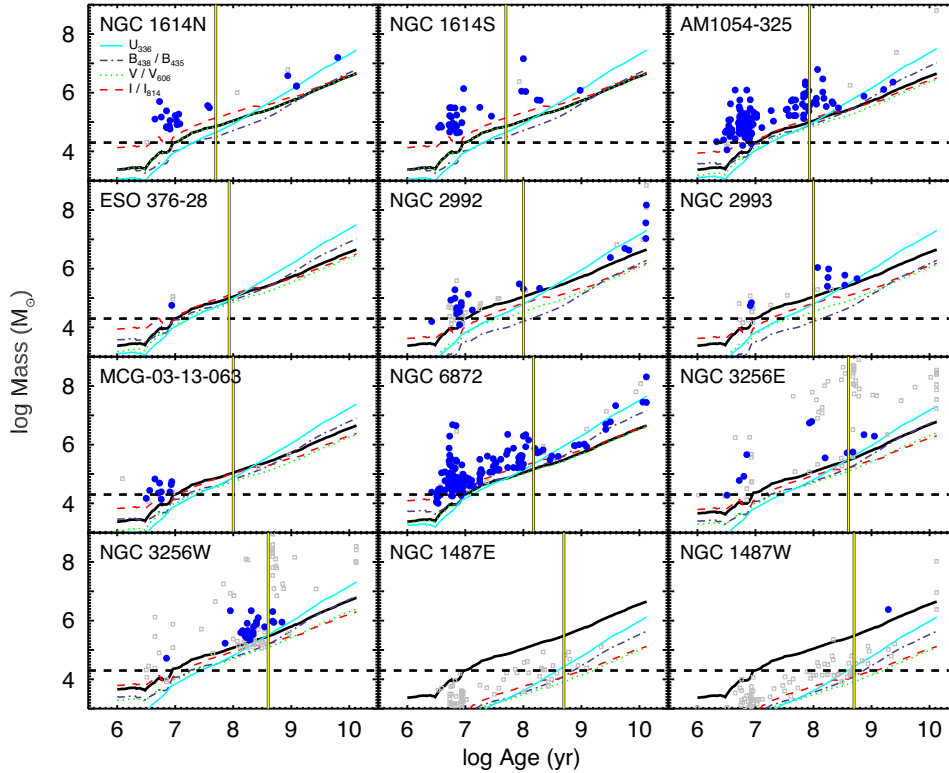
Figure 17. Ages and masses from Figs 3 to 14, compiled together. All systems except for NGC 1487 have at least one SCC with an age <10 Myr, indicating recent cluster formation. Both NGC 3256W and NGC 3256E show a number of non-SCC objects at the interaction age, with large masses. Their high masses, indicating bright absolute magnitudes, along with poor fits to our SSP model ($\chi^2 > 3$, Section 2.5) suggest these objects are foreground stars in the Milky Way. It is notable that these only appear in NGC 3256, which has the lowest Galactic latitude of our systems. They are not included in our SCC analysis.

4 RESULTS AND DISCUSSION

4.1 Mass function

A global mass function for all our systems is presented in Fig. 19. We stack our measured masses together for all our SCCs and plot them with bins of constant number, at 20 per bin, with 235 SCCs total. The mass bins are modelled as a power law with the form $dN/dM \propto M^\beta$. The slope, β, is found with a linear fit to log (dN/dM) with $\beta = -2.02 \pm 0.15$. The lower mass cut-off for our fit is at log $M = 4.6$ M$_\odot$, where the mass function begins to turnover. This turnover is caused by incompleteness at the lower mass limit. While some studies have suggested the mass function follows the form of a Schecter function (Bastian et al. 2012; Adamo et al. 2015; Messa et al. 2018), we see no turnover at high masses, leading us to conclude a power law is a good fit for our data.

The value of β has been measured for many other systems as well, with values ranging from $\approx -2.15 - -1.85$. Our result of $\beta = -2.02 \pm 0.15$ for our stacked distribution is consistent with these previous results. Varying the number of objects per bin finds values of β consistent with our stated value, with $\beta = 2.14 \pm 0.11$ and $\beta = 2.08 \pm 0.19$ for 10 and 30 objects per bin, respectively.

The low numbers of SCCs in each system means we cannot generate a useful mass function for each system. It is, however, useful to look at our two systems with the largest numbers of SCCs, AM1054-325, and NGC 6872. These contain 89 and 87 SCCs below 10 Myr, respectively. As these constitute more than half of the objects in our stacked mass function, it is possible that they have a heavy influence on the derived slope and form of the distribution. To ensure

we are not affected by this, we also look at the mass function while excluding objects from AM1054-325 and NGC 6872. In Fig. 19, we include these three cases to compare to our full, stacked function.

The peak of the function at log Mass = 4.6 M$_\odot$ is normalized to the stacked function, and vertically offset in steps of 0.75 dex to plot all functions on the same plot. We again plot data using bins of constant number, 10 for AM1054-325 and NGC 6872, and 7 for the excluded function. All cases are consistent with one another, and the stacked mass function as well, suggesting our more populous systems are not overinfluencing the stacked mass function.

As a separate check, we fit our data to a power law using the the IDL program `mspecfit.pro`, developed by Rosolowsky (2005). This uses a maximum-likelihood fitting technique to the cumulative distribution to find the slope of a power-law distribution, and factors in the individual errors in mass for each data point. It will perform a fit to a regular power law $N(M' > M) \propto M^\beta$ as well as determine the possibility of the cumulative distribution having the form of a truncated power law, given as $N(M' > M) \propto N_0[(M/M_0)^\beta - 1]$, where M_0 is the cut-off mass and N_0 is the number of objects more massive than $2^{1/\beta}M_0$. If $N_0 \lesssim 1$, then the distribution is best fit to a single power law. We fit the four data sets shown in Fig. 19 and find that $N_0 = 0.0 \pm 1.8$, 1.0 ± 2.0, 0.0 ± 0.8, and 0.0 ± 1.3 for our stacked mass function, AM1054-325, NGC 6872, and our excluded function, respectively. This suggests our data is best fit with a power-law distribution. We thus plot our cumulative distribution functions of our data in Fig. 20, along with the best-fitting values of β, using a standard power-law function. We find our results are consistent with that of our binned data within a standard deviation.
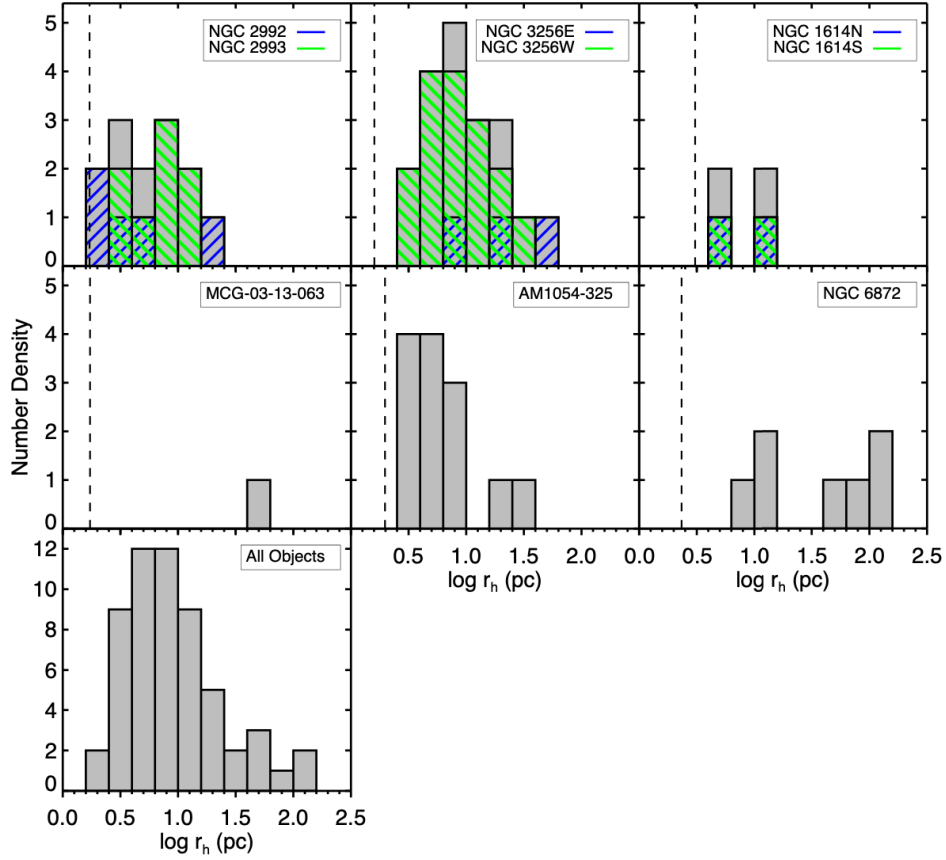
Figure 18. Half-light radii for our sources. Grey boxes indicate counts per bin for each system as a whole, while coloured lines represent individual tails (where applicable). The vertical dashed line represents the minimum size of an object able to be detected by ISHAPE (0.2 pix) in an image.
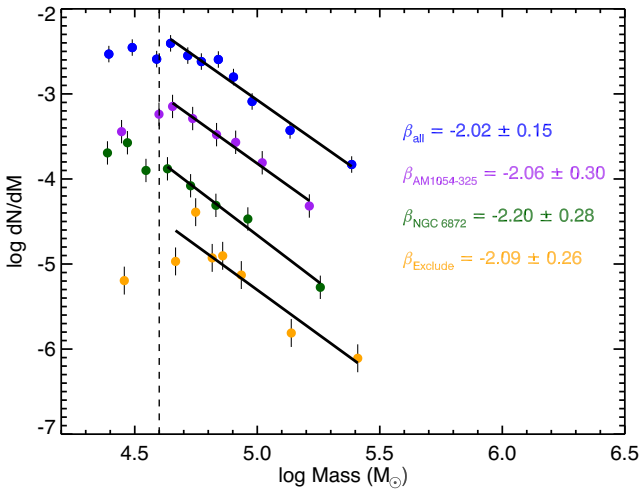

Figure 19. Mass functions for all, stacked objects (blue), AM1054-325 (purple), NGC 6872 (green), and stacked (orange), but excluding AM1054-325 and NGC 6872. Data are normalized to the stacked mass function and vertically offset to include all curves on the same plot. The corresponding fit slopes are shown on the right. While there is some scatter in β, all values are consistent with each other, within their uncertainties. Vertical dashed line indicates our cut-off mass at log Mass = 4.6.
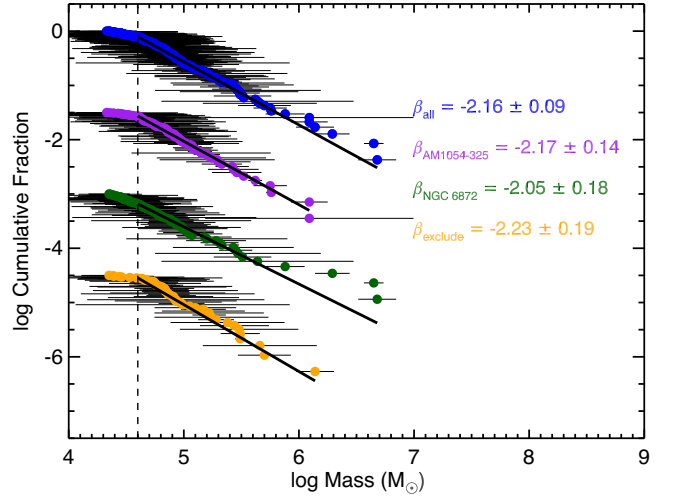
Figure 20. Cumulative mass distribution for stacked objects (blue), AM1054-325 (purple), NGC 6872 (green), and stacked (orange), but excluding AM1054-325 and NGC 6872. Data are vertically offset to include all curves on the same plot. The corresponding fit slopes are shown on the right. Values of β shown here are consistent with those from Fig. 19 to within a standard deviation. Horizontal grey bars indicate 1σ error bars for the individual mass points. Vertical dashed line indicates our cut-off mass at log Mass = 4.6.

Table 6. SFRs and CFE for our sample. CFE is determined by comparing the mass of clusters with ages below 10 Myr to the SFR within their respective tidal tail. The SFR is found using *GALEX* and *Swift* UV data, converted to an SFR (Kennicutt & Evans 2012).

System	SFR $(10^{-2} \, M_\odot \, yr^{-1})$	SFR$_{density}$ $(10^{-3} \, M_\odot \, yr^{-1} \, kpc^{-2})$	CFE (per cent)	A_{in} (kpc^2)	Σ_{SCC} (kpc^{-2})
ESO 376–28	0.55 ± 0.25	0.062 ± 0.028	$2.1^{+1.3}_{-0.6}$	88.9	-0.015 ± 0.013
NGC 2993	2.31 ± 0.15	0.129 ± 0.008	$1.11^{+0.70}_{-0.30}$	179.1	0.050 ± 0.017
NGC 2992	3.75 ± 0.21	0.163 ± 0.009	$3.5^{+2.3}_{-1.0}$	229.5	0.070 ± 0.022
NGC 3256E	6.30 ± 0.12	0.256 ± 0.005	$2.0^{+1.2}_{-0.5}$	246.0	0.034 ± 0.014
NGC 3256W	6.42 ± 0.11	0.321 ± 0.006	$0.17^{+0.11}_{-0.05}$	199.9	0.103 ± 0.025
NGC 1487E	0.428 ± 0.030	0.345 ± 0.024	N/A	12.4	0
NGC 1487W	0.493 ± 0.033	0.360 ± 0.024	N/A	13.7	0.073 ± 0.073
NGC 1614S	17.45 ± 0.40	0.532 ± 0.012	$5.0^{+3.2}_{-1.4}$	327.8	0.078 ± 0.019
NGC 6872	65.4 ± 3.0	0.734 ± 0.033	$5.7^{+3.7}_{-1.6}$	890.3	0.15 ± 0.016
MCG-03-13-063	0.98 ± 0.33	0.77 ± 0.26	$6.6^{+4.2}_{-1.8}$	12.8	0.76 ± 0.25
NGC 1614N	48.68 ± 0.14	1.598 ± 0.005	$0.66^{+0.42}_{-0.18}$	304.6	0.046 ± 0.017
AM1054–325	33.0 ± 3.1	2.55 ± 0.24	$6.9^{+4.4}_{-1.9}$	129.5	1.016 ± 0.090

4.2 Cluster formation efficiency

Stars form in clustered fashion, as seen in the Milky Way and in galaxies beyond (Zepf et al. 1999; Clarke, Bonnell & Hillenbrand 2000; Lada & Lada 2003; Bressert et al. 2010; Whitmore et al. 2010). Observational studies have attempted to determine how many stars are born in bound clusters by measuring the amount of star formation occurring in clusters, compared to the local region (e.g. Goddard, Bastian & Kennicutt 2010; Ryon et al. 2014; Adamo et al. 2015). The CFE is defined as the ratio of the cluster formation rate and the SFR (both in units of $M_\odot \, yr^{-1}$), so that CFE = CFR/SFR. Difficulty arises in the definition of 'bound' clusters, as internal and environmental processes are capable of disrupting and unbinding clusters (Portegies Zwart et al. 2010; Krumholz, McKee & Bland-Hawthorn 2019), requiring age limits for cluster analysis.

To match previous observations, we limit our SCC ages to 1–10 Myr. The SFR is measured from the UV flux of our *GALEX* and *Swift* images and converted to SFR using the following relation from Kennicutt & Evans (2012):

$$\log SFR \, (M_\odot \, yr^{-1}) = \log L_x - \log C_x, \qquad (1)$$

where L_x is luminosity (erg s^{-1}, and C_x is a calibration constant dependent on the observed wavelength (43.35 for *GALEX* FUV and 43.17 for *Swift uvm2*).

The CFR was found by summing the mass of all clusters with an age between 1 and Myr, and dividing by the time interval of 9 Myr. Completeness will affect the total mass of clusters that can be detected; low-mass clusters will not be observed in our images. We find the approximate mass of a 10 Myr old cluster with $M_V = -8.5$ (from our detection cut-off in Section 2.5) to be $\approx 10^{4.3} \, M_\odot$. We assume we are complete above this mass limit, and calculate the missing, or undetected mass, assuming the cluster mass function follows a power law with slope $\beta = -2.0$, extending from $100 \, M_\odot$ to $10^7 \, M_\odot$. We perform the same calculation with slopes of $\beta = -2.15$ and -1.85 for our upper and lower error bounds. For $\beta = -2.0$, -2.15, and -1.85, we find the total percentage of mass in clusters with masses greater than $10^{4.3} \, M_\odot$ to be 54 per cent, 33 per cent, and 74 per cent, respectively. Note that a shallower slope implies we measure a more complete sample of our clusters.

Our results are shown in Table 6. As NGC 1487W/E both do not contain clusters which fit our criterion, they do not have a corresponding CFE. The general trend is that systems with a higher
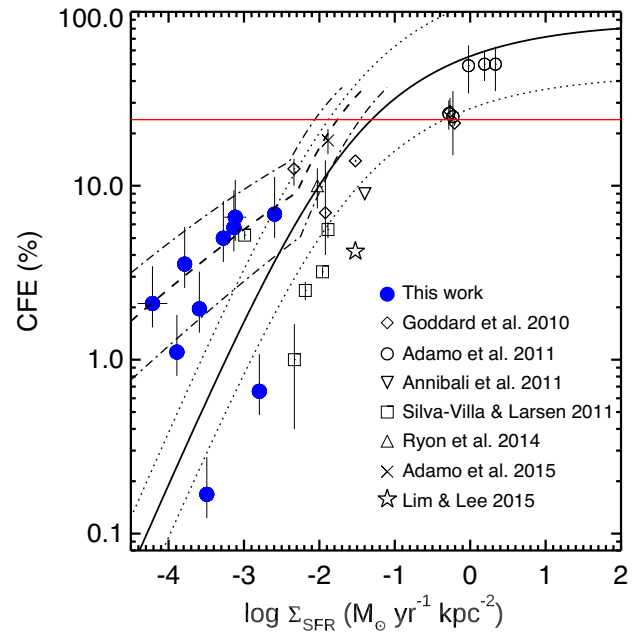

Figure 21. CFE plotted against the log SFR density. Included are several similar measurements gathered in Adamo et al. (2015), as well as a theoretical curve from Kruijssen (2012) in solid black. Dotted lines indicate a factor of 2 variation in the theoretical model. We include a modified version of the Kruijssen (2012) curve, using the Σ_{gas} versus Σ_{SFR} relation from Bigiel et al. (2008), as a dashed line. The dot–dashed lines indicate upper and lower limits on this relation as defined by Johnson et al. (2016). The red solid line corresponds to the 24 per cent value of CFE from Chandar et al. (2017).

SFR density (Σ_{SFR}) show more efficient cluster formation. Data are plotted in Fig. 21. We plot our data against a theoretical CFE from Kruijssen (2012) for comparison, with dotted lines indicating a variation factor of 2. This model predicts cluster formation to follow the surface gas density (Σ_{gas}), and therefore Σ_{SFR} via the Kennicutt–Schmidt law (Kennicutt 1998). The CFE tails off at high Σ_{SFR}. At the high-gas densities implied by the high Σ_{SFR} tidal interactions between neighbouring GMCs can impede cluster formation.

While the Kennicutt–Schmidt law assumes the relation between Σ_{gas} and Σ_{SFR} remains the same at all scales, this may not be the case. When studying star formation at sub-kpc scales, Bigiel et al. (2008)

found a decrease in Σ_{SFR} at low values of Σ_{gas}. This decrease is correlated with saturation of H I in the total gas content of the region (H I + H$_2$). This effect has been parametrized by Johnson et al. (2016), using a broken power law, to predict Σ_{SFR} based on Σ_{gas}. We include the CFE as a function of Σ_{SFR} based on this relation, again using the formulation from Kruijssen (2012), in Fig. 21 as a dashed line. The broken power-law formula manifests as a flattening of the curve at -2.3 in log Σ_{SFR}, corresponding to the gas environment being dominated by H I over H$_2$. Upper and lower limits provided by Johnson et al. (2016), derived from the Bigiel et al. (2008) data, are plotted as dot–dashed lines.

We find a good agreement with the Bigiel et al. (2008) curve, with only NGC 3256W and NGC 1614N falling more than 1σ below the lower limit. Notably, our data fall on the flattened part of the CFE curve, corresponding to an H I-dominated environment, suggesting the star-forming regions in our tails are primarily composed of HI over H$_2$.

We note that relation between the CFE and Σ_{SFR} was designed for a 'typical' spiral galaxy, and should be used as a rough estimate (Kruijssen 2012). In Fig. 21, we include data from previous surveys (Goddard et al. 2010; Adamo, Östlin & Zackrisson 2011; Annibali et al. 2011; Silva-Villa & Larsen 2011; Ryon et al. 2014; Adamo et al. 2015; Lim & Lee 2015) as compiled by Adamo et al. (2015). Our data extend to smaller Σ_{SFR} values than previously measured.

The dependence of the CFE on Σ_{SFR} has been questioned by Chandar et al. (2017), who studied several systems and found an average CFE of 24 per cent, independent of Σ_{SFR}. This constant value is indicated in Fig. 21 as a red horizontal line. They suggested that the variability seen in the CFE by other authors was caused by using different cluster age intervals for different galaxies in determination of the CFE. The result was a biased sampling of the CFE using a cluster age range of 0–10 Myr for systems with high Σ_{SFR}, and 10–100 Myr for systems with a low Σ_{SFR}. Indeed, we note that of the data points in Fig. 21, Adamo et al. (2011, 2015), Annibali et al. (2011), and Lim & Lee (2015) use objects with ages of 1–10 Myr, while the others use a range of ages from 1–10, 10–100, and 1–100 Myr in their CFE determinations. Our use of 1–10 Myr matches the majority of the listed studies. Independent of other studies, however, we find that our sample seems to match the theoretical model, and shows a trend of decreasing CFE with decreasing Σ_{SFR}.

4.3 Spatial distribution

SCC age and mass are plotted against distance from the centre of the interacting system in Figs 3–14. The central point of each system is obtained as coordinates from SIMBAD. The median distance is marked with a dashed vertical line. We perform KS tests on the age and mass distributions for our SCCs as separated by the median distance to the centre, with results shown in Table 7. We find statistically significant results beyond 2σ in only two tails: NGC 1614S and AM1054-325. NGC 1614S shows significant results in both its age and mass distributions, with p-values of 0.0011 and 0.0052 for its age and mass distributions, respectively. From Fig. 4, we see there is a clump of young objects near the base of the tail, with masses $\approx 10^5$ M$_\odot$. KS results for its companion tail, NGC 1614N, produce p-values of 0.18 and 0.06 for the age and mass distributions, respectively. We do not claim either of these results for NGC 1614N to be significant. AM1054-325 shows significant results in the mass distribution, but not in age.

For the majority of our sample, we see that the general trend shows a relatively even distribution of ages though the tidal debris; young

Table 7. KS results for age and mass distributions of SCCs in tails, between objects interior and exterior to the median distance to the centre of the system.

System	KS$_{Age}$	KS$_{Mass}$
NGC 1614N	0.18	0.06
NGC 1614S	0.0011	0.0052
AM1054-325	0.92	0.018
ESO 376–28	N/A	N/A
NGC 2992	0.27	0.56
NGC 2993	0.96	0.96
MCG-03-13-063	0.44	0.99
NGC 6872	0.68	0.89
NGC 3256E	0.85	0.45
NGC 3256W	0.91	0.66
NGC 1487E	N/A	N/A
NGC 1487W	N/A	N/A

objects are not concentrated in any particular region, but are found throughout the tidal tails.

4.4 Dynamical age

The dynamical age of a cluster (Π), introduced by Gieles & Portegies Zwart (2011), offers a method for estimating if a cluster is gravitationally bound at the current time. It is defined as the ratio of the age of a cluster to the crossing time of the cluster (T_{cr}):

$$\Pi \equiv \frac{t_{cluster}}{T_{cr}}. \tag{2}$$

T_{cr} is defined as

$$T_{cr} \text{ (s)} \equiv 10 \left(\frac{r_h^3}{GM} \right)^{1/2}, \tag{3}$$

where G is the gravitational constant, M is the mass of the cluster, and r_h is the half-light radius of the cluster. A cluster is said to be gravitationally bound if $\Pi \geq 1$. At this dynamical age, the stars in the cluster have evolved for longer than a crossing time, and as such are not likely to escape from the cluster, meaning the cluster is gravitationally bound. Objects with $\Pi < 1$ are not necessarily unbound, but as the stars have not yet evolved for longer than a crossing time, they still have time to escape before then, and we cannot determine if they are bound to the cluster. Unbound associations will expand with time, causing T_{cr} to increase as well, and remain at or below $\Pi = 1$. Bound objects, on the other hand, will remain bound and compact with time, causing Π to increase with time. Data for our SCCs are shown in Fig. 22.

The determination of a cluster as bound or unbound remains an estimate, as several factors will influence the evolution of a cluster. If the natal gas of a cluster is expelled too quickly, on a time-scale comparable to the crossing time, the cluster is more susceptible to disruption, for a given star formation efficiency (Hills 1980; Baumgardt & Kroupa 2007). Similarly, it is not possible for us to determine if a cluster, even with $\Pi > 1$, will remain bound throughout the lifetime of the merger, as this calculation does not take into account external forces. Clusters which passnearby GMCs or through the disc or nucleus of the merging galaxies are subject to gravitational tidal forces which can disrupt them (e.g. Spitzer 1958; Tacconi et al. 2008; Kim et al. 2018; Krumholz et al. 2019). However, as these objects exist in the diffuse regions of tidal debris, their chances of survival is increased as they will not experience the strong gravitational forces seen in the nuclear regions.
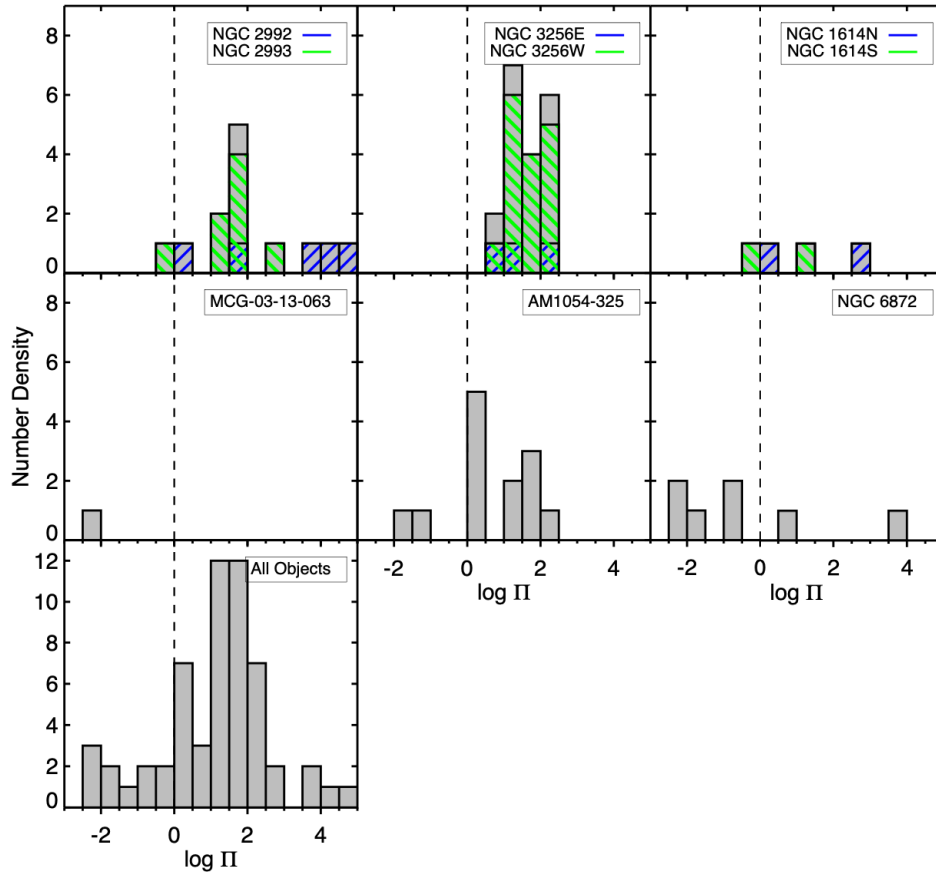
Figure 22. Dynamical ages of SCCs, following the prescription set by Gieles & Portegies Zwart (2011). The vertical dashed line marks the limit for gravitationally bound objects; those to the right of the line are gravitationally bound, while those to the left are unbound. Gray boxes indicate counts per bin for each system as a whole, while coloured lines represent individual tails (where applicable).

4.5 Age and mass as related to half-light radii

There is debate on the relation between cluster age and mass on their physical sizes. The initial half-light radius of a cluster is predicted, from an analytic model, to depend on the mass and gas surface density (Choksi & Kruijssen 2021). As clusters evolve, mass-loss and stellar interactions within the cluster will cause its expansion (Portegies Zwart et al. 2010). Gieles, Heggie & Zhao (2011) suggest two stages of radii evolution for clusters in tidal fields: expansion, driven by mass loss, followed by contraction. They find that two-thirds of the Milky Way's globular clusters are in the expansion phase.

Several studies of extragalactic clusters have found a slight dependence of age on radius (Lee, Chandar & Whitmore 2005; Bastian et al. 2012; Ryon et al. 2017), while others have found none (Larsen 2004; Scheepmaker et al. 2007; Brown & Gnedin 2021). There is a similar debate on the relation between mass and radius, and it is not clear that observational studies have found a relationship between these cluster properties (Ryon et al. 2017; Brown & Gnedin 2021). There is considerable scatter in the distribution of cluster radius, hiding any clear signals.

We plot the ages and masses of our SCCs against their radii in Fig. 23. We include both objects that are determined to be gravitationally bound and those which are not. We again find considerable scatter in our radii distribution, complicating any clear conclusions. On the left side of Fig. 23, we compare the ages of our SCCs to their radii. There are only a small number of objects at
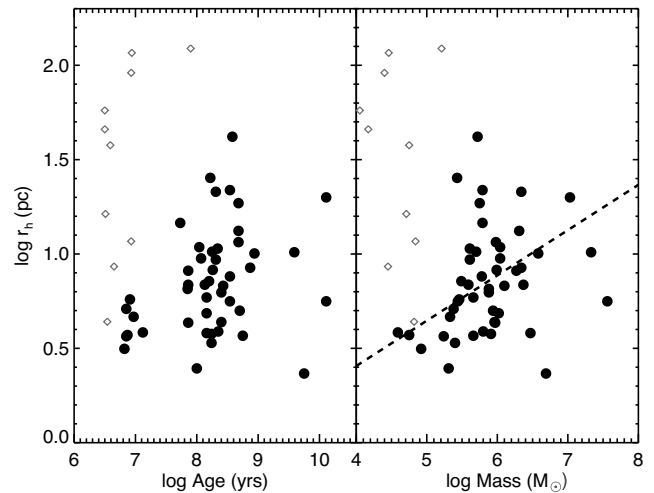

Figure 23. Half-light radii for our sources, as a function of age (*Left*) and mass (*Right*). Filled circles represent bound objects, while diamonds are unbound objects, using the definition set in Section 4.4. On the right, we include the mass–radius relation from Brown & Gnedin (2021). Our data are consistent with their model, but there is a large amount of scatter in our data.

ages <10 Myr, as a result of our selection criteria, namely that we look for isolated objects. Star clusters are formed in clustered fashion (Gieles, Bastian & Ercolano 2008; Bastian et al. 2009a; Gouliermis et al. 2015; Grasha et al. 2015), meaning our young SCCs will be in crowded regions which have been removed from our ISHAPE catalogue. This effect is seen in the fact that the young, unbound objects have large, extended radii, indicating blending. Thus, while Fig. 23 suggests that cluster radius increases with age, we have a small and biased sample at ages around 10 Myr.

Looking at the right panel of Fig. 23 we see the relation between our masses and radii. We again see a large amount of scatter in our data, with no clear trend. Recent work by Brown & Gnedin (2021) looked at the cluster radii of 31 galaxies from the Legacy Extragalactic UV Survey (LEGUS). LEGUS galaxies are nearby (<12 Mpc) spiral and irregular galaxies, with few interacting systems and no major mergers. Their work finds a power-law relation between mass and radius extending up to 10^5 $M_\odot$. Above this mass limit, the relation appears to flatten, though this may be the result of low numbers of clusters with these large masses. We overplot their fit in Fig. 23, continuing their trend to higher masses. We find our data are consistent with their fit, though there is large scatter.

4.6 NGC 1487 objects

NGC 1487 stands out from the rest of the mergers in our sample: it is three times closer than our next closest galaxy, there is only one SCC between the two tidal tails, and it has been classified as both a merger between two disc galaxies (Aguero & Paolantonio 1997) and a merger between dwarf galaxies (Bergvall, Laurikainen & Aalto 2003; Buzzo et al. 2021). Despite the lack of SCCs, visual examination of the tails shows an abundance of objects within the debris. This suggests the debris host faint, low-mass objects that belong to the merging system, but are not luminous, high-mass clusters with $M_V < -8.6$. The absence of high-mass objects may arise if this is indeed a merger between dwarf galaxies. Massive star clusters and high SFRs require high gas pressure (Blitz & Rosolowsky 2006; Zubovas et al. 2014; Maji et al. 2017), and these required pressures may not be produced in a dwarf galaxy merger. Lahén et al. (2019) were able to simulate a merger between two equal-sized dwarf galaxies, which produced clusters with masses $\geq 10^5$ $M_\odot$. Pressures in these clusters was found to be $\sim 10^7$ k (K cm^{-3})$^{-1}$, smaller than the 10^8–10^{12} k (K cm^{-3})$^{-1}$ values seen in simulations of major mergers (Maji et al. 2017).

To consider this scenario of low-mass cluster formation, we construct a stacked mass function with objects from both tails. We eliminate our magnitude limit, but still require that sources are fit to our SSP models with $\chi^2 \leq 3$ and $V_{606} - I_{814} < 1.43$. We only include objects with an age ≤ 10 Myr as before; results are shown in Fig. 24 for 58 objects that meet our requirements. We fit our data to the mass turnover at log Mass = 3.1, and find that our data shows a slope of $\beta = -2.06 \pm 0.31$. This is consistent with our results at higher masses for our SCCs, where the completeness limit only allowed a fit down to log Mass = 4.6.

Our SED modelling assumes a continuously populated IMF, which is a reasonable assumption for our clusters with masses >10^4 $M_\odot$. Below this mass limit, the stochastic sampling of the stellar IMF can affect photometric measurements (Larsen 2011). The low numbers of stars can mean that a cluster can host only single digit numbers of supergiants, or none at all. The overall colour of the cluster would become bluer in the absence of supergiants, causing us to underestimate the age; consequently, the mass can decrease as well, as younger clusters are more luminous than older ones. This can result in a bi-modality of colours in clusters (Popescu & Hanson
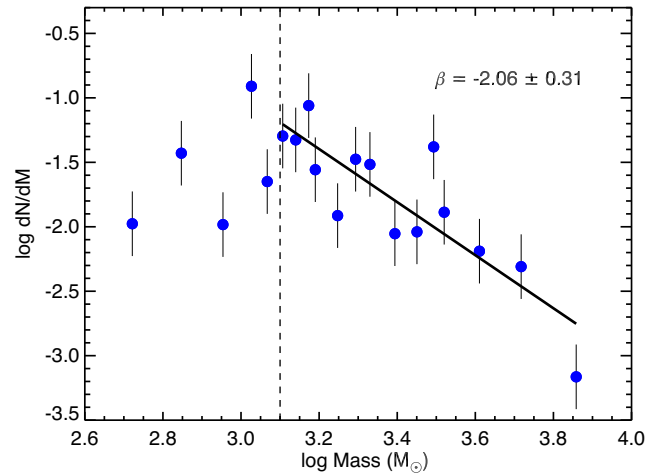

Figure 24. Mass function for sources in NGC 1487E and NGC 1487W. The dashed vertical line indicates our mass cut at log Mass = 3.1.
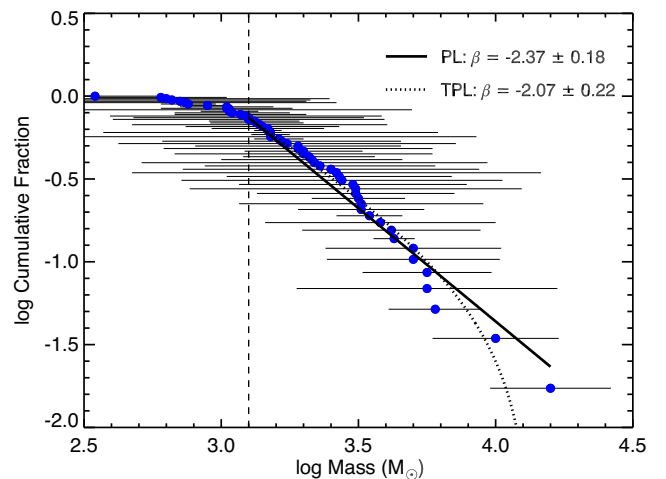

Figure 25. Cumulative fraction of sources in NGC 1487E and NGC 1487W. We overplot a power-law function as a solid black line, and a truncated power law as a dotted line.

2010; Silva-Villa & Larsen 2011). Despite this, the effect on the slope of the mass function β is small (Fouesneau et al. 2012), and eliminating sources with poor fits to models will reduce this effect (Fouesneau & Lançon 2010).

We plot the cumulative fraction of objects in Fig. 25, again using the MSPECFIT.PRO code to search for a truncated power law. We find for NGC 1487 a value of $N_0 = 3.7 \pm 3.6$, giving marginal significance ($\approx 1\sigma$) for a truncated power law. We plot both a standard power law and a truncated power law to our cumulative mass distribution in Fig. 25.

The similarities in slopes of our mass functions of NGC 1487 and stacked systems (see Figs 19 and 24, and Figs 20 and 25) imply we are observing the low-mass end cluster formation. We suggest that the pressure in NGC 1487 is too low to reach the threshold for massive clusters, as it is the result of mergers between dwarf galaxies, and not a major merger.

We look at the cluster radii of these objects as well, using ISHAPE. Neither tail in NGC 1487 contains enough foreground stars to produce a PSF image; we generate a PSF for each of the five B_{438}-band images in our sample (NGC 3256W, NGC 3256E,
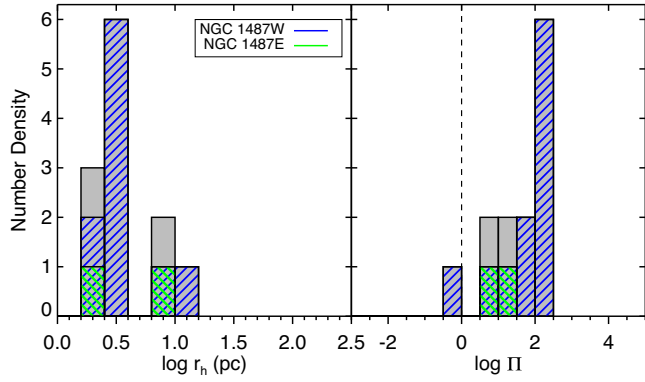
Figure 26. Half-light radii (*left*) and dynamical ages (*right*) for sources in NGC 1487W and NGC 1487E.
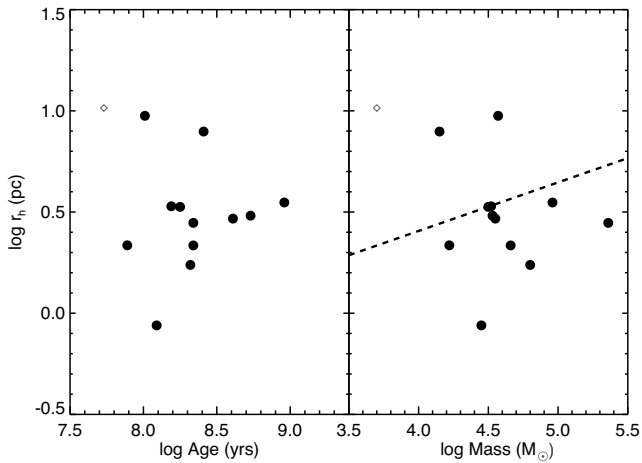

Figure 27. Same as Fig. 23, but for combined sources in NGC 1487E/W. We again include the mass–radius relation from Brown & Gnedin (2021).

NGC 6872, AM1054-325, and MCG-03-13-063), run ISHAPE five separate times, using each PSF once. Our final derived r_h value is the mean value from each run. We find the dynamical ages for these objects as well, as in Section 4.4. Results are shown in Fig. 26. All objects except for one in these tails are gravitationally bound, following Portegies Zwart et al. (2010). Fig. 27 shows the age and mass of these objects plotted against their radii. We again include the relation of Brown & Gnedin (2021) between mass and radius. Our data points show similar scatter as our SCCs, in Fig. 23.

Objects in NGC 1487 are more compact than in our other tails. The median half-light radius for bound sources in NGC 1487 is 3.03 pc, compared to 6.78 pc for all our other systems. We do not see the large, 10 pc clusters that exist in NGC 3256 or NGC 2992/3.

5 SUMMARY

We have analysed 425 SCCs in 12 tidal tails, across seven merging systems. We summarize our findings as follows:

(i) Many objects in tidal tails show signs of line emission in colour–colour diagrams, indicating young ages <10 Myr. Clusters at these ages will have strong emission in H α, which falls in our V_{606}-band filter. The effect of this emission impacts our colour–colour diagrams. These colours indicate current, ongoing star formation in tidal debris. The age and mass distributions (Fig. 17) suggest that

previous star formation episodes produced many more SCCs, as evidenced by high-mass objects seen at older ages.

(ii) The mass function of our SCCs has a consistent shape as compared to YMCs in other systems. Conventionally, the mass function of YMCs takes the form of a power law with a slope of $\beta \approx -2.0$. Other studies have found evidence of a high-mass cut-off, suggesting the mass function follows a Schecter function instead. We do not find evidence for such a mass cut-off, and find our data fit well to a power law with slope $\beta = -2.02 \pm 0.15$ using binned data, and $\beta = -2.16 \pm 0.09$ for a cumulative distribution fit.

(iii) The CFE in tidal tails increases as the SFR density increases. We use *GALEX* and *Swift* UV imaging to determine the SFR in our tails. When compared to previous observations and theoretical predictions using a reformulation of the Kennicutt–Schmidt law from Bigiel et al. (2008) and Johnson et al. (2016), we find good agreement, implying the gas in the tidal debris is primarily H I and that the CFE depends on the local environment. Our data pushed this link to lower SFR densities than previously observed for cluster formation.

(iv) Little dependence on galactic radii is seen for ages or masses of SCCs. Our KS tests reveal only NGC 1614S has significant differences in age or mass distributions with regard to galactocentric distance, while AM1054-325 shows significance in mass and distance only. Our other systems show that young clusters are distributed throughout the tails.

(v) Cluster radii of gravitationally bound objects, as determined using calculations from Portegies Zwart et al. (2010), fall in the range of 2–32 pc, with a median value of 7 pc. We do not see a relation between age and radius, or mass and radius. Work by Brown & Gnedin (2021) suggests cluster radius increases with mass; we include their power-law determination, which is consistent with our data.

(vi) Low-mass objects in NGC 1487, which fall below our magnitude limit of $M_V < -8.5$, show a mass function with a slope of $\beta = -2.00 \pm 0.28$ using binned data. We find minimal significance ($\approx 1\sigma$) for a truncated power law with slope $\beta = -2.07 \pm 0.22$, and a slope of $\beta = -2.37 \pm 0.18$ for a pure power law, using a cumulative distribution fit. Though the uncertainties are large, these values are consistent with our stacked SCC mass function, suggesting cluster formation is consistent down to low masses.

6 DATA AVAILABILITY

HST, *GALEX*, and *Swift* data are publicly available through the MAST portal at https://mast.stsci.edu/portal/Mashup/Clients/Mast/Portal.html. The derived data generated in this research will be shared on reasonable request to the corresponding author.

REFERENCES

Adamo A., Östlin G., Zackrisson E., 2011, MNRAS, 417, 1904
Adamo A., Kruijssen J. M. D., Bastian N., Silva-Villa E., Ryon J., 2015, MNRAS, 452, 246
Aguero E. L., Paolantonio S., 1997, AJ, 114, 102
Annibali F., Tosi M., Aloisi A., van der Marel R. P., 2011, AJ, 142, 129
Bastian N., Hempel M., Kissler-Patig M., Homeier N. L., Trancho G., 2005a, A&A, 435, 65
Bastian N., Gieles M., Efremov Y. N., Lamers H. J. G. L. M., 2005b, A&A, 443, 79
Bastian N., Gieles M., Ercolano B., Gutermuth R., 2009a, MNRAS, 392, 868
Bastian N., Trancho G., Konstantopoulos I. S., Miller B. W., 2009b, ApJ, 701, 607
Bastian N. et al., 2012, MNRAS, 419, 2606
Baumgardt H., Hilker M., 2018, MNRAS, 478, 1520
Baumgardt H., Kroupa P., 2007, MNRAS, 380, 1589
Bergvall N., Laurikainen E., Aalto S., 2003, A&A, 405, 31
Bigiel F., Leroy A., Walter F., Brinks E., de Blok W. J. G., Madore B., Thornley M. D., 2008, AJ, 136, 2846
Bik A., Lamers H. J. G. L. M., Bastian N., Panagia N., Romaniello M., 2003, A&A, 397, 473
Blitz L., Rosolowsky E., 2006, ApJ, 650, 933
Bressert E. et al., 2010, MNRAS, 409, L54
Brown G., Gnedin O. Y., 2021, MNRAS, 508, 5935
Buzzo M. L. et al., 2021, MNRAS, 503, 106
Chabrier G., 2001, ApJ, 554, 1274
Chandar R., Whitmore B. C., Dinino D., Kennicutt R. C., Chien L. H., Schinnerer E., Meidt S., 2016, ApJ, 824, 71
Chandar R., Fall S. M., Whitmore B. C., Mulia A. J., 2017, ApJ, 849, 128
Choksi N., Kruijssen J. M. D., 2021, MNRAS, 507, 5492
Clarke C. J., Bonnell I. A., Hillenbrand L. A., 2000, in Mannings V., Boss A. P., Russell S. S., eds, Protostars and Planets IV. Univ. Arizona Press, Tuscon, AZ, p. 151
Correnti M., Goudfrooij P., Bellini A., Girardi L., 2021, MNRAS, 504, 155
de Grijs R., Anders P., Zackrisson E., Östlin G., 2013, MNRAS, 431, 2917
Dolphin A. E., 2000, PASP, 112, 1397
Duc P. A., Brinks E., Springel V., Pichardo B., Weilbacher P., Mirabel I. F., 2000, AJ, 120, 1238
Elmegreen B. G., 2008, ApJ, 672, 1006
Elson R. A. W., Fall S. M., Freeman K. C., 1987, ApJ, 323, 54
English J., 2017, Int. J. Mod. Phys. D, 26, 1730010
English J., Freeman K. C., 2003, AJ, 125, 1124
Ennis A. I., Bassino L. P., Caso J. P., De Bórtoli B. J., 2019, MNRAS, 488, 770
Eufrasio R. T., Dwek E., Arendt R. G., de Mello D. F., Gadotti D. A., Urrutia-Viscarra F., Mendes de Oliveira C., Benford D. J., 2014, ApJ, 795, 89
Fedotov K., Gallagher S. C., Konstantopoulos I. S., Chandar R., Bastian N., Charlton J. C., Whitmore B., Trancho G., 2011, AJ, 142, 42
Fedotov K., Gallagher S. C., Durrell P. R., Bastian N., Konstantopoulos I. S., Charlton J., Johnson K. E., Chandar R., 2015, MNRAS, 449, 2937
Fouesneau M., Lançon A., 2010, A&A, 521, A22
Fouesneau M., Lançon A., Chandar R., Whitmore B. C., 2012, ApJ, 750, 60
Gallagher S. C. et al., 2010, AJ, 139, 545
Gieles M., Portegies Zwart S. F., 2011, MNRAS, 410, L6
Gieles M., Bastian N., Ercolano B., 2008, MNRAS, 391, L93
Gieles M., Heggie D. C., Zhao H., 2011, MNRAS, 413, 2509
Goddard Q. E., Bastian N., Kennicutt R. C., 2010, MNRAS, 405, 857
Gouliermis D. A. et al., 2015, MNRAS, 452, 3508
Grasha K. et al., 2015, ApJ, 815, 93

Herrero-Illana R., Alberdi A., Pérez-Torres M. Á., Alonso-Herrero A., González-Millán D., Pereira-Santaella M., 2017, MNRAS, 470, L112
Hills J. G., 1980, ApJ, 235, 986
Holtzman J. A., Burrows C. J., Casertano S., Hester J. J., Trauger J. T., Watson A. M., Worthey G., 1995, PASP, 107, 1065
Hopkins P. F., Cox T. J., Hernquist L., Narayanan D., Hayward C. C., Murray N., 2013, MNRAS, 430, 1901
Horellou C., Koribalski B., 2007, A&A, 464, 155
Jarrett T. H. et al., 2006, AJ, 131, 261
Jog C. J., Solomon P. M., 1992, ApJ, 387, 152
Johnson L. C. et al., 2016, ApJ, 827, 33
Jordán A. et al., 2007, ApJS, 171, 101
Kennicutt R. C. J., 1998, ARA&A, 36, 189
Kennicutt R. C., Evans N. J., 2012, ARA&A, 50, 531
Kim J.-h. et al., 2018, MNRAS, 474, 4232
King I., 1962, AJ, 67, 471
Knierman K. A., Gallagher S. C., Charlton J. C., Hunsberger S. D., Whitmore B., Kundu A., Hibbard J. E., Zaritsky D., 2003, AJ, 126, 1227
Konstantopoulos I. S. et al., 2010, ApJ, 723, 197
Krabbe A. C., Rosa D. A., Dors O. L., Pastoriza M. G., Winge C., Hägele G. F., Cardaci M. V., Rodrigues I., 2014, MNRAS, 437, 1155
Kroupa P., 2001, MNRAS, 322, 231
Kruijssen J. M. D., 2012, MNRAS, 426, 3008
Krumholz M. R., McKee C. F., Bland-Hawthorn J., 2019, ARA&A, 57, 227
Lada C. J., Lada E. A., 2003, ARA&A, 41, 57
Lahén N., Naab T., Johansson P. H., Elmegreen B., Hu C.-Y., Walch S., 2019, ApJ, 879, L18
Larsen S. S., 1999, A&AS, 139, 393
Larsen S. S., 2004, A&A, 416, 537
Larsen S. S., 2011, in Stellar Clusters and Associations: A RIA Workshop on Gaia, Granada, Spain. p. 75
Larsen S. S., Romanowsky A. J., Brodie J. P., 2021, A&A, 651, A102
Lee H. J., Lee M. G., 2005, J. Korean Astron. Soc., 38, 345
Lee M. G., Chandar R., Whitmore B. C., 2005, AJ, 130, 2128
Leitherer C. et al., 1999, ApJS, 123, 3
Lim S., Lee M. G., 2015, ApJ, 804, 123
Lípari S., Díaz R., Taniguchi Y., Terlevich R., Dottori H., Carranza G., 2000, AJ, 120, 645
Lípari S. L. et al., 2004, MNRAS, 354, L1
Machacek M. E., Nulsen P., Stirbat L., Jones C., Forman W. R., 2005, ApJ, 630, 280
Maji M., Zhu Q., Li Y., Charlton J., Hernquist L., Knebe A., 2017, ApJ, 844, 108
Marigo P., Girardi L., Bressan A., Groenewegen M. A. T., Silva L., Granato G. L., 2008, A&A, 482, 883
Matsui H., Tanikawa A., Saitoh T. R., 2019, PASJ, 71, 19
Mengel S., Lehnert M. D., Thatte N. A., Vacca W. D., Whitmore B., Chandar R., 2008, A&A, 489, 1091
Messa M. et al., 2018, MNRAS, 473, 996
Mihos J. C., Bothun G. D., Richstone D. O., 1993, ApJ, 418, 82
Mulia A. J., Chandar R., Whitmore B. C., 2015, ApJ, 805, 99
Mulia A. J., Chandar R., Whitmore B. C., 2016, ApJ, 826, 32
Mullan B. et al., 2011, ApJ, 731, 93
Olsson E., Aalto S., Thomasson M., Beswick R., 2010, A&A, 513, A11
Osterbrock D. E., 1989, Astrophysics of Gaseous Nebulae and Active Galactic Nuclei. University Science Books, Herndon, VA
Pang X., Li Y., Tang S.-Y., Pasquato M., Kouwenhoven M. B. N., 2020, ApJ, 900, L4
Popescu B., Hanson M. M., 2010, ApJ, 713, L21
Portegies Zwart S. F., McMillan S. L. W., Gieles M., 2010, ARA&A, 48, 431
Randriamanakoto Z., Väisänen P., Ryder S. D., Ranaivomanana P., 2019, MNRAS, 482, 2530
Renaud F., 2018, New A Rev., 81, 1
Renaud F., Bournaud F., Duc P.-A., 2015, MNRAS, 446, 2038
Risaliti G., Gilli R., Maiolino R., Salvati M., 2000, A&A, 357, 13
Rodruck M. et al., 2016, MNRAS, 461, 36
Roming P. W. A. et al., 2009, ApJ, 690, 163

Rosa D. A., Dors O. L., Krabbe A. C., Hägele G. F., Cardaci M. V., Pastoriza M. G., Rodrigues I., Winge C., 2014, MNRAS, 444, 2005

Rosolowsky E., 2005, PASP, 117, 1403

Ryon J. E. et al., 2014, AJ, 148, 33

Ryon J. E. et al., 2017, ApJ, 841, 92

Salpeter E. E., 1955, ApJ, 121, 161

Salzer J. J., Jangren A., Gronwall C., Werk J. K., Chomiuk L. B., Caperton K. A., Melbourne J., McKinstry K., 2005, AJ, 130, 2584

Sanders D. B., Soifer B. T., Elias J. H., Madore B. F., Matthews K., Neugebauer G., Scoville N. Z., 1988, ApJ, 325, 74

Sani E. et al., 2008, ApJ, 675, 96

Scheepmaker R. A., Haas M. R., Gieles M., Bastian N., Larsen S. S., Lamers H. J. G. L. M., 2007, A&A, 469, 925

Schlafly E. F., Finkbeiner D. P., 2011, ApJ, 737, 103

Schweizer F., 1987, in Faber S. M., ed., Nearly Normal Galaxies. From the Planck Time to the Present. Springer, New York, p.18

Silva-Villa E., Larsen S. S., 2011, A&A, 529, A25

Spitzer L. J., 1958, ApJ, 127, 17

Stetson P. B., 1987, PASP, 99, 191

Tacconi L. J. et al., 2008, ApJ, 680, 246

Toomre A., Toomre J., 1972, ApJ, 178, 623

Trancho G., Bastian N., Schweizer F., Miller B. W., 2007a, ApJ, 658, 993

Trancho G., Bastian N., Miller B. W., Schweizer F., 2007b, ApJ, 664, 284

Trancho G., Konstantopoulos I. S., Bastian N., Fedotov K., Gallagher S., Mullan B., Charlton J. C., 2012, ApJ, 748, 102

Väisänen P., Rajpaul V., Zijlstra A. A., Reunanen J., Kotilainen J., 2012, MNRAS, 420, 2209

Weilbacher P. M., Duc P. A., Fritze-v. Alvensleben U., 2003, A&A, 397, 545

Whitmore B. C., Schweizer F., 1995, AJ, 109, 960

Whitmore B. C., Schweizer F., Leitherer C., Borne K., Robert C., 1993, AJ, 106, 1354

Whitmore B. C. et al., 2010, AJ, 140, 75

Yuan H. B., Liu X. W., Xiang M. S., 2013, MNRAS, 430, 2188

Zepf S. E., Ashman K. M., English J., Freeman K. C., Sharples R. M., 1999, AJ, 118, 752

Zubovas K., Sabulis K., Naujalis R., 2014, MNRAS, 442, 2837

APPENDIX A: NOTES ON INDIVIDUAL TAILS

A1 NGC 1614N/S

This is our furthest merger in our sample, at a distance of 65.6 Mpc. The tidal debris are the youngest of our systems, forming 50 Myr after the second passage of the two galaxies (Väisänen et al. 2012). It boasts two tidal tails, with the northern tail wrapping back onto the centre of the merger, and the southern tail extended radially outward. This system has a large IR luminosity, with $L_{IR} = 4 \times 10^{11}$ $L_{\odot}$, classifying it as an LIRG. The large IR luminosity appears to be driven through star formation. A 300 pc ring surrounding the nucleus shows evidence of luminous H II regions as revealed in Pa-α observations. This ring also coincides with 3 μm PAH emission and radio continuum (Väisänen et al. 2012).

X-ray observations initially suggested the presence of an obscured AGN (Risaliti et al. 2000). However, L-band observations of the nucleus do not show any enhanced emission (Väisänen et al. 2012) as is characteristic of an AGN (Sani et al. 2008). The X-ray emission can be explained through low-mass x-ray binaries (LMXBs; Olsson et al. 2010). Most notably, high resolution VLBI observations do not find a compact source in the nucleus (Herrero-Illana et al. 2017). Should an AGN exist in NGC 1614, it is faint and turned off.

Figs 3 and 4 show the colour–colour diagrams of the SCCs in each tail. At a glance, the two tails in the same system appear different from each other. The southern tail has several objects with blue colours at $V_{606} - I_{814} < 0$, which do not appear in the northern tail. This is reflected somewhat in the age distributions for the two tails, as the

southern tails has several more young (<10 Myr) SCCs than seen in the northern tail. However, the difference in $V_{606} - I_{814}$ colour can be explained if internal extinction is affecting the northern clusters.

A KS test between the two tails for their SCC $U_{336} - B_{435}$, $B_{435} - V_{606}$, and $V_{606} - I_{814}$ colours gives p-values of 0.71, 1.3×10^{-5}, and 5.2 x 10^{-9}, respectively. A KS test between their ages and masses gives p-values of 0.049 and 0.69, respectively.

KS test results for NGC 1614S between in-tail and out-of-tail SCCs for $U_{336} - B_{435}$, $B_{435} - V_{606}$, and $V_{606} - I_{814}$ colours give p-values of 0.65, 0.045, and 1.2×10^{-4}, respectively. For NGC 1614N, we find p-values of 0.17, 0.19, and 7.2×10^{-3} for $U_{336} - B_{435}$, $B_{435} - V_{606}$, and $V_{606} - I_{814}$. Cluster excess for NGC 1614S and NGC 1614N are 0.078 ± 0.019 kpc^{-2}, and 0.046 ± 0.017 kpc^{-2}, respectively. NGC 1614S has a cluster excess above 3σ, though NGC 1614N does not.

A2 AM1054-325 and ESO 376–28

AM1054-325 and ESO 376–28 are an interacting pair in a relatively early stage of their merger history, with an interaction age of 85 Myr. AM1054-325 is a spiral galaxy with an elongated spiral arm extending to the North and a tidal dwarf galaxy (TDG) candidate to the NE (Weilbacher, Duc & Fritze-v. Alvensleben 2003). Spectroscopic measurements find H II regions in AM1054-325, created by shocked gas (Krabbe et al. 2014), including some within the tidal dwarf galaxy, as well as in the outer disc and extended spiral arm. Its interacting companion, ESO 376–28, is a lenticular galaxy. Krabbe et al. (2014) finds emission lines indicative of H II regions within this galaxy as well.

ESO 376–28 contains only one SCC, with an age of $10^{6.5}$ yr and a mass of $10^{4.75}$ $M_{\odot}$, about 3.6 kpc from the centre of the galaxy. Unfortunately, we cannot derive a radius due to its low S/N in ISHAPE.

While ESO 376–28 is devoid of SCCs, its companion, AM1054-325, hosts the largest excess of SCCs in our sample, at 1.016 ± 0.090 kpc^{-2}. A KS test of colours for in-tail and out-of-tail SCCs gives p-values of 0.166, 4.5×10^{-3}, and 2.0×10^{-8} for $U_{336} - B_{438}$, $B_{438} - V_{606}$, and $V_{606} - I_{814}$, respectively. We find p-values less than 0.04 for our $B_{438} - V_{606}$ and $V_{606} - I_{814}$ colours, indicating our in-tail and out-of-tail SCCs are drawn from differing distributions. This is largely due to the young ages of the in-tail SCCs, as seen in the colour–colour diagram in Fig. 5. Many objects have evidence of emission from recombination lines of hydrogen, notably H α, strongly influencing the V_{606}-band magnitudes. The spatial distribution in Fig. 5 shows that the young, <10 Myr SCCs are distributed through the length of the tidal tail. Mixed in with the young SCCs, we see a group of older and more massive objects, with ages between 10^8 and $10^{8.5}$ and masses between $10^{5.5}$ and 10^6 $M_{\odot}$. These appear clustered around the TDG candidate, with ages similar to the age of the interaction of the system; this region may have seen the first burst of star formation from the encounter.

From Fig. 5, there appear to be two groupings of ages, one at 6.7 and one at 7.9. It is tempting to interpret this as two isolated bursts of star formation; however, it is possibly an indication of continuous star formation since the encounter, and we are instead seeing artificial effects due to age fitting. Similar artifacts are seen in other cluster studies (see Section 3.3).

The system is at a distance of 52.9 Mpc and is compact, with each galaxy filling one quadrant of the WFC3 FOV. This causes crowding to be a concern when fitting radii, and we eliminated about a third of our SCCs. SCCs which were fit show radii between ~3 and 10 pc. All but one of the 13 sources are gravitationally bound.

A3 NGC 2992/3

NGC 2992 and 2993 are disc galaxies in the initial stages of merging. This interaction has produced a tidal tail in NGC 2993 and a tidal dwarf galaxy at the northern tip of NGC 2992. A tidal bridge, connecting the two main galaxies, is not imaged in our data. Our *HST* observations fall on the tidal tail of NGC 2993, and the TDG and associated tidal debris, North of the main body of NGC 2992.

NGC 2992 contains an AGN and is classified as a Seyfert 1.9. The classification has changed over time, as the AGN has shown variability, though observations from 2007 to 2014 indicate it may have become stable. The luminosity in the nuclear region appears to be dominated by the AGN, with low contributions from star formation. Dynamical models from Duc et al. (2000) place the interaction at 100 Myr.

This system was observed in parallel observing mode, with ACS B_{435} and WFC3 U_{336} imaging. Due to the observing constraints, our U_{336}-band imaging is not as deep as our other systems (see Section 2.6) and has several more undetected objects in U_{336}, resulting in upper limits in Figs 7 and 8.

A KS test between the SCCs for the two tails for their $U_{336} - B_{438}$, $B_{438} - V_{606}$, and $V_{606} - I_{814}$ colours gives p-values of 0.011, 0.16, and 1.2×10^{-3}, respectively. A KS test between their ages and masses gives p-values of 0.40 and 0.47, respectively. This indicates the SCCs in both tails are consistent with being drawn from the same distribution. The difference in KS results between colours and masses/ages can be explained if the SCCs have internal extinction, resulting in different colours, but similar masses and ages.

A KS test between SCC colours for in-tail and out-of-tail SCCs in NGC 2992 finds p-values of 0.73, 0.87, and 0.50 for $U_{336} - B_{435}$, $B_{435} - V_{606}$, and $V_{606} - I_{814}$, respectively. The fact that none of these values are below 0.04 means we cannot say that SCCs are drawn from different populations. However, the SCC excess is 0.070 ± 0.022 kpc^{-2}, above 3σ. Thus, while the colours of in-tail and out-of-tail SCCs are similar, the strong excess of objects inside the tidal debris lends us confidence that these are not containment sources. NGC 2993 shows no SCCs out-of-tail, with 9 in-tail SCCs. While there are no out-of-tail SCCs to compare to, visual examination of Fig. 8 shows an absence of detected objects (SCCs and non-SCCs) in the out-of-tail region, above $U_{336} - B_{438} = -0.5$, suggesting objects in NGC 2993 are real.

The median SCC radius for the two tails is 5.6 pc, with all but one of our objects being bound. At the tip of the tail in NGC 2993 we find a massive, extended cluster, with age of $10^{8.1}$ yr, mass of $10^{6.0}$ M$_\odot$, and a radius of 9.5 pc.

A4 MCG-03-13-063

MCG-03-13-063 is a disturbed spiral with no optical companion. Little data exists on this system. It features an extended spiral arm, hosting beads of clusters. The SCCs are recently formed, with ages <10 Myr. The arm is thin, with clusters located in well-defined regions Mullan et al. (2011).

Our KS tests for $U_{336} - B_{438}$, $B_{438} - V_{606}$, and $V_{606} - I_{814}$ find p-values of 2.1×10^{-3}, 0.35, and 1.7×10^{-3}, respectively, for in-tail and out-of-tail SCCs. The SCC excess in this system is 0.76 ± 0.25 kpc^{-2}, significant beyond 3σ.

A5 NGC 6872

NGC 6872 is a disturbed barred spiral galaxy merging with the nearby, smaller galaxy IC 4970. It is located in the Pavo Group with 12 other members. The interaction has produced two elongated spiral arms which span a distance of 160 kpc from east to west (Eufrasio et al. 2014). Our study here focuses only on the eastern tidal arm of the system; we do not image the western tail. An X-ray view of the Pavo Group found a trail of *x*-ray emission between NGC 6872 and the large, dominant elliptical galaxy NGC 6876. The origin of this trail is unlikely to be related to tidal interactions, as the morphology of NGC 6876 does not show any disturbances. Furthermore, no H I is seen associated with the *x*-ray emission (Horellou & Koribalski 2007). Rather, it is likely due to a Bondi–Hoyle wake; as NGC 6872 passes through the IGM, gas is gravitationally focused in its wake, and is compressed and heated (Machacek et al. 2005; Horellou & Koribalski 2007).

NGC 6872 has been modelled by Mihos, Bothun & Richstone (1993) and Horellou & Koribalski (2007), finding that the tidal arms can be reproduced in an interaction with a small companion, at a mass ratio of 5:1. While models from Mihos et al. (1993) predict enhanced star formation in the nucleus of the galaxy, H α observations show a lack of star formation in the interior; rather, the star-forming regions are located in the tidal arms.

An isolated blue clump can be seen at the northern tip of the eastern tail in *GALEX* imaging, which unfortunately falls outside our FOV. This clump is a possible TDG, though spectroscopic analysis is needed to confirm that it is gravitationally bound (Eufrasio et al. 2014).

NGC 6872 hosts the largest numbers of SCCs in our sample, with 158 in the tail, and an excess of 0.150 ± 0.016 kpc^{-2}. KS tests between in-tail and out-of-tail SCCs find p-values of 0.026, 0.049, and 0.025 for $U_{336} - B_{438}$, $B_{438} - V_{606}$, and $V_{606} - I_{814}$, respectively. Young SCCs are found throughout the tail, from the base to the tip, suggesting this system is currently undergoing a burst of star formation. Our KS tests show that there is no statistical difference between ages or masses of SCCs with distance. However, we see a visual trend for SCCs with ages $> 10^8$, where older SCCs are preferentially within our 41 kpc median distance. To a lesser extent, this extends to masses $> 10^6$, with more massive clusters located closer to the centre. Radii are difficult to determine as with NGC 1614, due to the large distance (62.6 Mpc) and crowding. We find radii for seven SCCs, with only two of them being bound objects.

Our results are similar to a ground-based study of the entire body of NGC 6872, which found young clusters (<10 Myr) and objects around 10^6 M$_\odot$ in both of the tidal tails of the system (Bastian et al. 2005a). They also did not find any objects older than 145 Myr in the tails; these resided in the interior of the galaxy. Although we have found SCCs older than this in our tidal tail, the majority are less than this age: 18 out of the 158 SCCs are older than 145 Myr.

A6 NGC 3256E/W

NGC 3256 has an IR emission of $L_{\rm IR} = 3.3 \times 10^{11} L_\odot$ (Lípari et al. 2004), classifying it as an LIRG. This is a starbursting galaxy with two prominent tidal tails.

The central 5 kpc of the system shows three compact knots, one at optical wavelengths and the other two in IR, as well as an asymmetric spiral arm associated with each individual source, suggesting this system is the result of three galaxies merging together. The likely scenario involves two disc galaxies merging first, followed by a smaller, satellite galaxy merging (Lípari et al. 2000, 2004).

The interior shows prodigious amounts of star formation, powering a galactic wind and the system's large IR luminosity (Lípari et al. 2000). This is visualized in bright H II regions (Lípari et al. 2000; English & Freeman 2003) and numerous young, blue clusters (Zepf et al. 1999; Goddard et al. 2010; Mulia, Chandar & Whitmore 2016).

Broad-band analysis of such objects shows the age distributions have an overdensity of objects with ages less than 10 Myr (Goddard et al. 2010; Mulia et al. 2016). Spectroscopy of several of these internal clusters also shows they have a high metallicity, at $Z \sim 1.5\ Z_\odot$ (Trancho et al. 2007b). Similarly, three clusters in the Western tidal tail studied spectroscopically show similar elevated metallicity levels of $Z \sim 1.5\ Z_\odot$ (Trancho et al. 2007a).

SCCs for both NGC 3256W and NGC 3256E do not show the large numbers of young objects seen in the nucleus. There are only four in the eastern tail and one in the Western tail that fall below an age of 10 Myr. Populations of SCCs in both tails have ages comparable to the interaction age of 400 Myr, suggesting they formed in the interaction. Rodruck et al. (2016) find similar results for ages of the diffuse light as well. This is also seen in Mulia, Chandar & Whitmore (2015), who looked at clusters in NGC 3256E, at the base of the tail, near the nucleus. The ages of these objects were weakly clustered around 250 Myr.

A KS test between the SCCs for the two tails for their $U_{336} - B_{438}$, $B_{438} - V$, and $V - I$ colours gives p-values of 0.017, 2.2×10^{-4}, and 8.3×10^{-3}, respectively. A KS test between their ages and masses gives p-values of 0.05 and 2.0×10^{-4}, respectively. The KS tests show differences between the masses of the clusters, though not the ages. NGC 3256E appears to be currently forming clusters, as also seen in Rodruck et al. (2016).

KS tests for in-tail and out-of-tail SCCs give similar results for both tails. For NGC 3256E, we find p-values of 0.92, 0.17, and 0.23 for $U_{336} - B_{438}$, $B_{438} - V$, and $V - I$, respectively. For NGC 3256W, we find p-values of 0.97, 0.33, and 0.18 for $U_{336} - B_{438}$, $B_{438} - V$, and $V - I$, respectively. The cluster excess for NGC 3256E is 0.034 ± 0.014 kpc^{-2}, and 0.103 ± 0.025 kpc^{-2} for NGC 3256W. The excess in NGC 3256W is above 3σ.

SCCs in NGC 3256 show a median radius of 8.5 pc, larger than the typical radii of clusters in extragalactic observations, which generally peak around 3–5 pc (Jordán et al. 2007; Bastian et al. 2012; Chandar et al. 2016; Ryon et al. 2017; Ennis et al. 2019). However, these other studies still see objects with large radii, and such large objects are expected to form in galaxy mergers (Renaud, Bournaud & Duc 2015). All sources for which we have a measured radius appear to be bound, from Fig. 22. Of particular note is a massive object located near the tip of the tail, with age $10^{8.3}$ yr, mass $10^{6.3}$ M$_\odot$, and a radius of 10.7 pc. This is our fourth largest SCC in NGC 3256W, and is 50 kpc from the centre of the merging system. This object could evolve to become similar to a present day globular cluster. Clusters formed in tidal tails can migrate outwards and become isolated globular clusters (Matsui, Tanikawa & Saitoh 2019).

NGC 1487 stands out from the rest of the mergers in our sample: it is three times closer than our next closest galaxy, there is only one SCC between the two tidal tails, and it has been classified as both a merger between two disc galaxies (Aguero & Paolantonio 1997) and a merger between dwarf galaxies (Bergvall et al. 2003; Buzzo et al. 2021). Despite the lack of SCCs, visual examination of the tails shows an abundance of objects within the debris. This suggests the debris host faint, low-mass objects that belong to the merging system, but are not luminous, high-mass clusters with $M_V < -8.6$. The absence of high-mass objects may arise if this is indeed a merger between dwarf galaxies. Massive star clusters and high SFRs require high-gas pressure (Blitz & Rosolowsky 2006; Zubovas et al. 2014; Maji et al. 2017), and these required pressures may not be produced in a dwarf galaxy merger. Lahén et al. (2019) were able to simulate a merger between two equal sized dwarf galaxies, which produced

clusters with masses $\geq 10^5$ M$_\odot$. Pressures in these clusters was found to be $\sim 10^7$ k(K cm^{-3})$^{-1}$, smaller than the $10^8 - 10^{12}$ k(K cm^{-3})$^{-1}$ values seen in simulations of major mergers (Maji et al. 2017).

A7 NGC 1487E/W

NGC 1487 is our nearest merging system in our sample, at 10.8 Mpc. This is a peculiar system in that it has been called a disc merger (Aguero & Paolantonio 1997) and a dwarf merger (Bergvall et al. 2003; Buzzo et al. 2021). Aguero & Paolantonio (1997) classify it as a merger between disc galaxies due to emission line strength, which gives a SFR higher than seen in isolated galaxies. Lee & Lee (2005) give an age for the merger at 500 Myr, as BI-band photometry of star clusters in the nucleus suggests they are 500 Myr. This age estimate is supported by integral field spectroscopy (Buzzo et al. 2021). However, these estimates are based on the assumption that the age of the interaction is correlated to the number density peak in cluster age, implying that they formed due to the interaction. It is possible that the present tidal tails could have formed in a secondary encounter between the galaxies, and thus have a younger age than the quoted value.

Evidence of a dwarf merger is seen in its low mass ($4.6 \pm 1.2 \times 10^9$ M$_\odot$) and low mass of nuclear concentrations ($\sim 1.5 - 0.2 \times 10^9$ M$_\odot$), similar velocity fields between concentrations, and low SFRs (Buzzo et al. 2021).

Tidal debris extends to the East and West. Most interestingly, it is the only galaxy in our sample not to contain high-mass clusters. As discussed in Section 4.6, NGC 1487 may be a dwarf galaxy merger, and not able to produce the necessary pressures to form massive clusters, as seen in major mergers. We find only one SCC in NGC 1487W, and none in NGC 1487E. The rest of the detected objects fall below our magnitude cut of $M_V < -8.5$. This does not mean that it does not contain star clusters, but rather it does not contain high-mass clusters. Despite the lack of SCCs, both regions of debris show clear excesses of detected objects, as compared to their respective out-of-tail regions. The cluster excesses for in-tail vs out-of-tail sources is 4.2 ± 0.6 for NGC 1487W, and 3.3 ± 0.6 for NGC 1487E, which are statistically significant for each tail.

The mass function for objects in the debris shows a similar slope as our SCCs (Fig. 24), though with smaller radii (Fig. 26). The implication is that we are seeing the low-mass regime of cluster formation in NGC 1487. We are able to see these objects despite their faintness as NGC 1487 is relatively nearby (10.8 Mpc). Three clusters in the central region observed by Mengel et al. (2008) show similar properties to what we see in the tidal tails, with radii between 1 and 3 pc and masses between 7×10^4 and 15×10^4 M$_\odot$. H I observations show high densities, at $2.55 \pm 0.51 \times 10^7$ M$_\odot$ kpc^{-2}, but Mullan et al. (2011) suggest this may be an inclination effect.

The ages of objects found in the tails closely resemble previous studies of star formation in NGC 1487. Lee & Lee (2005) found a bimodal distribution in the colours of star clusters, which correspond to ages of 15 and 500 Myr. Buzzo et al. (2021) find the star formation history of the system to have peaks at ~ 10 and ~ 300 Myr. Our data in the tails show objects with ages <10 Myr, as well as a clustering of objects at 500 Myr, matching the star formation history of the tails to the interior.

This paper has been typeset from a TEX/LATEX file prepared by the author.